

Near infrared spectroscopy of M dwarfs. III. Carbon and oxygen abundances in late M dwarfs including the dusty rapid rotator 2MASSI J1835379+325954 *

Takashi TSUJI

Institute of Astronomy, School of Science, The University of Tokyo, 2-21-1 Osawa, Mitaka-shi, Tokyo, 181-0015
ttsuji@ioa.s.u-tokyo.ac.jp

and

Tadashi NAKAJIMA

National Astronomical Observatory of Japan, 2-21-1 Osawa, Mitaka-shi, Tokyo, 181-8588
tadashi.nakajima@nao.ac.jp

(Received ; accepted)

Abstract

Carbon and oxygen abundances of eight late M dwarfs are determined based on the near infrared spectra of medium resolution ($R = \lambda/\Delta\lambda \approx 20000$). In late M dwarfs, dust forms in their photospheres for T_{eff} below about 2600 K, and this case applies to the M8.5 dwarf 2MASSI J1835379+325954 (hereafter 2MASS 1835+32) whose T_{eff} is 2275 K. Other seven objects with T_{eff} above 2600 K are analyzed with the dust-free models. For the case of 2MASS 1835+32 analyzed by the dusty model, the surface temperature is higher by about 600 K due to the blanketing effect of the dust grains, mainly composed of iron grains, and the carbon and oxygen abundances are higher by about 0.25 and 0.15 dex, respectively, compared to the analysis by the dust-free model. Once dust forms in the photosphere, the dust works as a kind of thermostat and temperatures of the surface layers remain nearly the same as the condensation temperatures of the dust grains. For this reason, the temperatures of the surface layers of the dusty dwarfs are relatively insensitive to the fundamental parameters including T_{eff} . In addition, it appears that 2MASS 1835+32 is a rapid rotator, for which its EWs are thought to remain unchanged by the rotational broadening. This is, however, true only when the true continuum is well defined. Otherwise, the pseudo-continuum level depends on the rotational velocity and hence the EWs as well. For this reason, the derived abundances depend on the rotational velocity assumed: For the values of $V_{\text{rot}}\sin i = 37.6$ and 44.0 km s^{-1} available in the literature, the derived carbon and oxygen abundances differ by 0.23 and 0.14 dex, respectively, and we find that the higher value provides a better account of the observed spectrum. The resulting carbon and oxygen abundances in the eight late M dwarfs show no systematic difference from our results for the early and middle M dwarfs, and confirm the higher $A_{\text{O}}/A_{\text{C}}$ ratio at the lower metallicity. In late M dwarfs, CO and H₂O remain as excellent abundance indicators of carbon and oxygen, respectively, except for additional uncertainty due to the complexity associated with the dust formation in the latest M dwarfs.

Key words: Stars: abundances – Stars: atmospheres – Stars: dust – Stars: low mass – Stars: rotation

1. Introduction

The late M dwarfs are the last stars that shine by their own nuclear burning in their interiors and mark the end of the main sequence. It was shown that the lower limit of the stellar mass that maintains the high enough central temperature to ignite hydrogen burning is $0.08 M_{\odot}$ (Hayashi & Nakano 1963; Kumar 1963). In recent years, more attention is directed to the objects below the hydrogen-burning limit, referred to as brown dwarfs, rather than to the lowest mass hydrogen-burning objects, the latest M dwarfs. At the end of the 20-th century, extensive searches for a brown dwarf have been attempted by several groups with different methods, and

a genuine brown dwarf, Gliese 229B, was finally discovered by Nakajima et al. (1995) with immediate spectroscopic verification by Oppenheimer et al. (1995). Since then, many brown dwarfs were discovered by the large scale surveys such as DENIS (Epchtein et al. 1999), 2MASS (Skrutskie et al. 2006), SDSS (York et al. 2000), UKIDSS (Lawrence et al. 2007), and WISE (Wright et al. 2010).

In observations, however, it is by no means easy to determine the stellar mass accurately, and hence it is not very sure if some latest M dwarfs are really stars or young brown dwarfs. Anyhow, some of our objects are situated at the boundary between stars and brown dwarfs, and we hope that a detailed spectroscopic study of such objects at relatively high resolution would be of some use in extending detailed spectroscopic analyses to very low mass objects. In fact, the high resolution spectroscopy was al-

* Based on data collected at Subaru Telescope, which is operated by the National Astronomical Observatory of Japan.

ready applied to a cool brown dwarf more than a decade ago by Smith et al. (2003), who observed the nearby T dwarf ϵ Indi Ba with the resolution as high as $R \approx 50000$ and showed the advantages of the high resolution spectroscopy over the other works mostly based on low resolutions. Thus, the very cool dwarfs including brown dwarfs are already within the capability of the present-day high resolution infrared spectroscopy and we are even too late to work on M dwarfs.

Now, returning to M dwarfs, one problem in the latest M dwarfs is that dust may form in their photospheres. In fact, it was shown that the thermochemical conditions for the formation of dust grains such as corundum, iron, and enstatite are well met in the photospheres of M dwarfs with T_{eff} below about 2600 K, and actual model photospheres in thermal and convective equilibria incorporating the dust formation have been generated (Tsuji et al. 1996a). The predicted spectra based on the dusty models appeared to be consistent with the known observation of the infrared spectrum of the latest M dwarf LHS 2924, while the dust-free models predicted H_2O bands to be too deep compared with the observed spectrum.

The evidence for dust has more clearly been shown in a peculiar cool dwarf GD 165B discovered by Becklin & Zuckerman (1988). This object showed a very red color but molecular bands were not so strong as expected for a possible low temperature suggested by the very red color. Such a characteristic could have been explained nicely by our dusty model (Tsuji et al. 1996b): The very red color is due to infrared excess caused by dust, which also weakens the molecular absorption bands at the same time. This object was later recognized as a brown dwarf and regarded as the proto-type of L type dwarfs (Kirkpatrick et al. 1999). Also an analysis of optical spectra has shown additional spectroscopic evidence for dust in late M dwarfs (Jones & Tsuji 1997). Since then the problem of the dusty photospheres has been studied mostly in connection with brown dwarfs both observationally and theoretically (e.g., see an extensive survey of such efforts by Helling et al. 2008a). More recently, modeling of the cool dwarfs has made significant progress, extending to the cooler brown dwarfs and extra-solar planets (see reviews, e.g., Helling & Casewell 2014; Marley & Robinson 2015) on one hand, and also to self-consistent cloudy models of late M and L dwarfs (Witte et al. 2011) on the other.

In addition to the problem of dust, some of the late M dwarfs are known to be rapid rotators. One of our targets 2MASS 1835+32, which was recognized as a nearby late-type M dwarf only recently (Reid et al. 2003), is also found to be a rapid rotator (Reiners & Basri 2010; Deshpande et al. 2012). In late M dwarfs in which molecular lines are already blended each other, the rapid rotation further smears out the blended spectra. We have developed a method to analyze the spectrum without the true-continuum by referring to the pseudo-continuum which is depressed appreciably by molecular bands (Tsuji & Nakajima 2014; Tsuji et al. 2015, hereafter Papers I and II, respectively). We find that our method can be extended quite well to the case of the pseudo-continuum

smeared-out further by the rapid rotation, and also can be applied to determine the rotational velocity more consistently.

In this paper, we first introduce our observed data (section 2) and then we discuss fundamental parameters such as effective temperatures of late M dwarfs (section 3). We then generate model photospheres including the dusty case, and examine the effect of dust on the thermal structures and spectra with our simple dusty models (section 4). We first analyze seven non-rapid rotators, whose effective temperatures are found to be above 2600 K and hence can be assumed to be dust-free (section 5). Then, we examine the rotational broadening on the spectrum of 2MASS 1835+32 (section 6). We examine the effects of dust formation, rotational velocity, and fundamental parameters on our abundance analysis (section 7). Finally, we discuss our results on the carbon and oxygen abundances in M dwarfs, dust in late M dwarfs, and the coolest end of the main sequence (section 8).

2. Observations

We observed eight late M dwarfs between M4.5 and M8.5 listed in table 1. Observations were carried out at the Subaru Telescope on 2014 August 31 (UT) using the echelle mode of the Infrared Camera and Spectrograph (IRCS) (Kobayashi et al. 2000) with adaptive optics. Six of the eight targets were bright enough in the visible to be natural guide stars, while LP 412-31 and 2MASS 1835+32 were too faint and laser guide stars were used. The slit width of $0.14''$ was sampled at $55 \text{ mas pixel}^{-1}$, and the resolution was about 20000 at K . The echelle setting was “ K^+ ”, which covered about a half of the K window with the orders, wavelength segments, and pixel-wise dispersions given in table 2. The targets were nodded along the slit, and observations were taken in an ABBA sequence, where A and B stand for the first and second positions on the slit. The total exposure time ranged from 24s (GJ 873) to 80 min (LP 412-31). The night was photometric at the beginning, but the condition gradually degraded and it was spectroscopic toward the end of the night. The visible seeing was better than $0.5''$ throughout the night. Near the mid night, a rapidly rotating B8V star, HR 326 was observed as the calibrator of telluric transmission. Signal-to-noise ratios of reduced spectra are given for the 28th and 25th orders in table 1. H_2O and CO lines are analyzed in the 28th order (aperture 2), and H_2O lines are also analyzed in the 25th order (aperture 5).

Data reduction was carried out using the standard IRAF¹ routines in the `imred` and `echelle` packages. After extraction of one-dimensional spectra, wavelength calibrations were calculated using telluric absorption lines in the spectra of HR 326. After wavelength calibrations of one-dimensional spectra of A and B positions, they were co-added to produce combined spectra. The combined spec-

¹ IRAF is distributed by the National Optical Astronomy Observatory, which is operated by the Association of Universities for Research in Astronomy, Inc., under cooperative agreement with the National Science Foundation.

tra were normalized by the pseudo-continuum levels and then calibrated for telluric absorption using the spectra of HR 326.

table 1: p.29
table 2: p.29

3. Fundamental parameters

Angular diameter measurement by interferometry is not yet extended to late M dwarfs, and we apply the $M_{3.4} - \log T_{\text{eff}}$ ($M_{3.4}$ is the absolute magnitude at $3.4 \mu\text{m}$ based on the WISE data (Wright et al. 2010)) relation introduced in Paper I, with a slight modification for the latest M dwarfs.

3.1. Effective temperatures

For the M dwarfs with $M_{3.4} \lesssim 9.0$ (dM4.5 – dM6) in our present sample, effective temperatures are estimated by the use of the $M_{3.4} - \log T_{\text{eff}}$ relation shown by the dashed line on figure 1 of Paper I (a part of which is reproduced in figure 1a by a dashed line). This method works well for these M dwarfs and the results for four objects, GJ 54.1, 873, 1002, and 1245B, are given in table 3.

For the later M dwarfs of $M_{3.4} > 9.0$ (dM7 – dM8.5), however, a dashed line (figure 1a) used to estimate T_{eff} was defined only by four objects, GJ 406, 644C, 752B and 3849, whose effective temperatures were determined by the infrared flux method (Tsuji et al. 1996a). We estimate the physical parameters of these four objects in table 4 and examine the results in comparison with those of the evolutionary models by Baraffe et al. (1998). As shown in the lower right corner of the HR diagram in figure 17 of Paper I and reproduced in figure 1b, three of these four objects (GJ 406, 644C, and 3849) agree well with the theoretical HR diagram by Baraffe et al. (1998) shown by a solid line. However, one object (GJ 752B) deviates appreciably from the theoretical HR diagram. For this reason, we adopt these three objects (GJ 406, 644C, and 3849) as reliable calibration objects, and use these three objects to define a revised $M_{3.4} - \log T_{\text{eff}}$ relation shown by a solid line in figure 1a. The resulting values of T_{eff} based on the revised $M_{3.4} - \log T_{\text{eff}}$ relation are given in table 3 for GJ 752B, GAT 1370, LP 412-31, and 2MASS 1835+32.

figure 1: p.15

table 3: p.29
table 4: p.30

3.2. Surface gravities

For estimating the surface gravity, radius and mass are needed. For this purpose, the effective temperature vs. radius relation given by equation 8 and the mass vs. radius relation given by equation 10 of Boyajian et al. (2012)

are applied to the dM4.5 - dM6 dwarfs and the results are given in table 3 together with the resulting values of $\log g$.

For the later dM7 - dM8.5 dwarfs, we try to extend the relations of Boyajian et al. (2012) by the use of our calibration stars in table 4. For this purpose, the mass is estimated with the use of the mass-luminosity (M_K) relation by Delfosse et al. (2000) extended to the lower masses ($M \lesssim 0.1 M_\odot$) with the use of the theoretical mass - M_K relation by Baraffe et al. (1998), as shown in figure 2. This extension should be reasonable, since the empirical (dashed line) and theoretical (dotted line) mass-luminosity relations agree very well for $M > 0.1 M_\odot$ in figure 2.

With the observed bolometric flux based on the photometry, the bolometric luminosity is derived with the known parallax, and with the T_{eff} based on the infrared flux method, the radius is estimated. The radius vs. effective temperature relation given by equation 8 of Boyajian et al. (2012) shown by a dashed line in figure 3 is extended to the lower temperatures with our calibration stars nos. 1, 2, and 4 in table 4, as shown by a solid line in figure 3. It is to be noted that our empirical data for three calibration stars agree rather well with the theoretical relation based on the evolutionary models of the solar metallicity (Baraffe et al. 1998) shown by a dotted line in figure 3.

The radius vs. mass relation given by equation 10 of Boyajian et al. (2012) shown by a dashed line in figure 4 is extended to the lower masses ($M \lesssim 0.1 M_\odot$) with the use of the calibration stars nos. 1, 2, and 4 in table 4, as shown by a solid line in figure 4. The dashed and solid lines are joined at $M \approx 0.15 M_\odot$. For comparison, predicted relation by the evolutionary models of the solar metallicity (Baraffe et al. 1998) is shown by a dotted line in figure 4. Again the empirical relation based on our three calibration objects agrees rather well with the theoretical result of Baraffe et al. (1998).

Now, radii and masses of our late M dwarfs are estimated with the use of the solid lines in figures 3 and 4, respectively, and the results for GJ 752B, GAT 1370, LP 412-31, and 2MASS 1835+32 are given in table 3 together with the resulting values of $\log g$.

figure 2: p.15

figure 3: p.15

figure 4: p.15

4. Model photospheres of late M dwarfs

We apply dust-free model photospheres for the M dwarfs with $T_{\text{eff}} \gtrsim 2600 \text{ K}$ (subsection 4.1). Since our sample now includes the latest M dwarf in which dust may form, we examine dusty models in some detail (subsection 4.2), and effects of dust on the thermal structures (subsection 4.3) and spectra (subsection 4.4) are discussed.

4.1. Dust-free model photospheres of M dwarfs

The T_{eff} values of our seven program stars are higher than 2600 K (table 3), and we apply the dust-free models of case C to these seven objects. The case C includes Ca series based on the abundance *case a* (see Table 1 of Tsuji 2002) adopting the classical solar C and O abundances (Anders & Grevesse 1989) and Cc series on the abundance *case c* adopting the downward revised C and O abundances (Allende Prieto et al. 2002). In our first iteration on CO spectra, we use the models of the Ca series from our UCM (Unified Cloudy Model) database². For further iterations, we generate specified model for each object based on T_{eff} and $\log g$ given in table 3, and the models are either Ca or Cc series depending on the carbon abundance determined by the first iteration on CO (section 5). These models are designated as Ca or Cc/ $T_{\text{eff}}/\log g$: for example, Ca3160c508 implies a model of Ca series, $T_{\text{eff}} = 3160$ K, and $\log g = 5.08$. The micro-turbulent velocity is kept to be 1 km s^{-1} throughout.

4.2. Dusty model photospheres of the latest M dwarfs

Dust may form in the photosphere of M dwarfs with $T_{\text{eff}} \lesssim 2600$ K (Tsuji 2002) and, since the T_{eff} value of our object 2MASS 1835+32 is found to be 2275 K (table 3), we consider the effect of dust in our analysis of this M8.5 dwarf. In late M dwarfs, however, dust formation has just started and only small amount of dust grains should be formed. For this reason, we assume the simplest LTE (local thermodynamical equilibrium) model that dust forms everywhere so long as temperature is lower than the condensation temperature, T_{cond} ($T \lesssim T_{\text{cond}}$), and we referred to such a model as a fully dusty model of case B (Tsuji 2002). However, such a fully dusty model of case B is most difficult from the viewpoint of generating non-grey convective models, possibly because very large dust opacities compared with the gaseous opacities dominate throughout the upper layers. For this reason, we could not complete a grid for case B before, but computed only one sequence of $\log g = 5.0$ (Tsuji 2002). We now need to generate some models of case B for the analysis of our target star and we consider this problem again in this section.

We are using a simple iterative procedure by correcting the temperature gradient by

$$\left(\frac{dT}{d\tau}\right)_{\text{rev}} = \frac{\sigma T_{\text{eff}}^4 - \pi F_{\text{conv}}(\tau)}{\pi F_{\text{rad}}(\tau)} \left(\frac{dT}{d\tau}\right), \quad (1)$$

where $F_{\text{rad}}(\tau)$, $F_{\text{conv}}(\tau)$, and $dT/d\tau$ are the total radiative flux, convective flux based on the local mixing-length theory (e.g., Henyey et al. 1965), and temperature gradient of a model at hand, respectively. Then, the revised temperature gradient $(dT/d\tau)_{\text{rev}}$ is integrated with several trial surface temperatures at $\log \tau_0 = -7.0$ (τ_0 is the optical depth defined by the continuous opacity at $\lambda = 0.81 \mu\text{m}$), and a revised $T(\tau)$ is fixed so that it gives the correct

surface flux of $\pi F_{\text{rad}}(\tau = 0) = \sigma T_{\text{eff}}^4$ (Tsuji 1966). This method was extended from the case neglecting convection, i.e., $F_{\text{conv}}(\tau) = 0$ (Tsuji 1965) and has an obvious meaning: The temperature gradient should be increased (decreased) if the total flux is smaller (larger) than the equilibrium value of σT_{eff}^4 . If convection is included, temperature gradient is tempered to be consistent with the smaller radiative flux, according to equation 1.

If dust forms, such an iterative procedure turns out to be unstable, possibly because very large dust opacities are highly sensitive to the changes of the physical conditions in general and also appear suddenly at $T = T_{\text{cond}}$. In such a case, we find that it is useful to temper the variation of $F_{\text{rad}}(\tau)$ somewhat. We prepare a small grid of the fully dusty models of case B to be applied to late M dwarfs; for T_{eff} between 2000 and 2600 K, $\log g = 5.0, 5.25$, and 5.5 , and abundances of *case a* and *case c*. The results are added to our UCM database². We generally aim at a flux constancy within 1 %, but flux errors as large as 3 % remain in cooler models near $T_{\text{eff}} = 2000$ K in case B³.

4.3. Effect of dust on the thermal structures

In figure 5, the thermal structures of the fully dusty models (blue or black) are compared with those of the dust-free models (light sky or grey) for $T_{\text{eff}} = 2600, 2300$, and 2000 K (abundance *case c* and $\log g = 5.25$). The condensation lines of corundum (Al_2O_3), iron (Fe) and enstatite (MgSiO_3) are shown by dashed lines. The dust-free models penetrate to the regime of $T \lesssim T_{\text{cond}}$ in the surface layers and the thermodynamical condition for dust formation is fulfilled in all the models shown in figure 5. Thus corundum first forms and temperatures are elevated somewhat by its blanketing effect. Then iron forms, and because of the larger abundance of iron, it has dominant effect: the temperatures of the upper layers coincide with the condensation line of iron as shown in figure 5. This is a result that the photosphere is forced to be in radiative equilibrium, and it seems that iron works as a kind of thermostat; if a temperature T_f within the condensation line of iron in our model is increased by perturbation, then the iron grains will evaporate and the temperature will decrease because the blanketing effect of the iron grains disappears. But, if the temperature goes down below T_f , iron grains form and the temperature will increase again because of the blanketing effect of the iron grains. Such processes repeat and the temperature will eventually settle at the starting value T_f . As a result, the temperatures converge to the condensation line of iron and the thermal structures of the dusty models in the surface layers are not much different for late M dwarfs of different effective temperatures, in marked contrast to the dust-free models in which surface temperatures show large differences for different effective temperatures, as shown in figure 5. It is to be noted, however, that enstatite could not be formed

² UCM is a kind of semi-empirical cloudy model, but our UCM database includes dust-free models (case C) as well as fully dusty models (case B) as its subsets. As for detail: <http://www.mtk.ioa.s.u-tokyo.ac.jp/~ttsuji/export/ucm2>.

³ The convergence in the fully dusty models of case B for $T_{\text{eff}} < 2000$ K is more difficult as shown for these models in a sequence of $\log g = 5.0$ so far computed². The models of case B, however, are no longer useful for $T_{\text{eff}} < 2000$ K and, instead, the cloudy models should be used for L and T dwarfs.

since the photospheres are warmer than the condensation temperatures of enstatite because of the blanketing effect of iron and corundum.

figure 5: p.16

4.4. Effect of dust on the spectra

The predicted spectra based on the dusty and dust-free models discussed in the previous subsection are shown in figure 6. In the model spectra of $T_{\text{eff}} = 2600$ K shown in the top of figure 6, the difference of the dusty (shown by blue or black) and dust-free (light sky or grey) cases is rather minor: the dusty model shows slightly weaker absorption only in the regions of strong absorption (e.g., at $2.5 \mu\text{m}$) because of its higher surface temperature. Although the temperatures of the surface region are about 400 K higher in the dusty model than in the dust-free model (see figure 5), the matter density in the surface region is very low and this region has little effect on the emergent spectra except for the very strong absorption formed in the very surface. For this reason, we neglect the effect of dust for M dwarfs with $T_{\text{eff}} \approx 2600$ K (e.g., GJ 752B, LP 412-31).

In the model spectra of $T_{\text{eff}} = 2300$ K shown in the middle of figure 6, the effect of dust is considerable, since the larger part of the surface region is now warmer (by about 600 K) in the dusty model than in the dust-free model (see figure 5). Especially, strong bands such as H_2O 1.9 and $2.7 \mu\text{m}$ bands as well as CO first overtone bands formed in the surface layers suffer appreciable effect, while weak lines such as at $2.2 \mu\text{m}$ region formed in the deeper layers show minor change. However, dust has considerable effect even on the weak lines on the higher resolution spectra, as will be shown in section 7.

In the case of $T_{\text{eff}} = 2000$ K shown in the bottom of figure 6, the effect of dust is more drastic: The spectrum of the dusty model shows overall excess compared with the dust-free model in the K band region and this is of course compensated for by the large extinction due to dust in the shorter wavelength region. The very strong absorption bands due to H_2O and CO in the dust-free model are much weaker in the dusty model because of the elevated temperatures in the larger part of the photosphere and also by the dust extinction. But $T_{\text{eff}} = 2000$ K is already in the regime of L dwarfs, and late M dwarfs are still free from such drastic effect of dust.

figure 6: p.16

5. Seven M dwarfs of non-rapid rotators

Seven M dwarfs in our sample except for 2MASS 1835+32 are not rapid rotators and also the effect of dust may not be important ($T_{\text{eff}} > 2600$ K). Then, CO and H_2O lines are analyzed by the mini curves-of-growth (subsection 5.1) and by the synthetic

spectra (subsection 5.2), as in Papers I and II.

5.1. The mini curve-of-growth analysis

5.1.1. First iteration on the CO blends

We analyze the CO blends of the 2-0 band listed in table 7 of Paper I with the solar carbon abundance of *case a* as an initial starting value for each object. Equivalent widths (EWs) are measured by referring to the pseudo-continuum and the resulting values of $\log W/\lambda$ are given in table 5. We then apply the mini curve-of-growth (CG) method from the beginning (i.e., not apply the conventional analysis as used in the first iteration on CO in Paper I).

The mini CG method was developed through our Papers I to II: Briefly summarizing, we first generate synthetic spectra for an assumed initial abundance $\log A_0$ and corrected abundances $\log A_0 \pm \delta$. Then, equivalent widths, W 's, are evaluated from these synthetic spectra by the same way as the observed EWs are measured, referring to the pseudo-continuum which is evaluated accurately by the use of the recent line-list of H_2O (Barber et al. 2006, Rothman et al. 2010). In the first iteration, we apply the models from the UCM grid and assume $\delta = 0.3$. Then we measure equivalent widths, W 's, on the predicted spectra calculated with the starting initial values of $\log A_C = -3.40$ ⁴ and $\log A_O = -3.08$ (*case a* for the initial model of Ca series) and with $\log A_C = -3.40 \pm \delta$ and $\log A_O = -3.08 \pm \delta$ ($\delta = 0.3$)⁵. These EWs are designated as $\log W(\delta)/\lambda$. Then, we generate a mini CG plotting $\log W(\delta)/\lambda$ against $\delta = -0.3, 0.0$, and $+0.3$ for each blend. With this mini CG, observed EW is converted to the abundance correction to the assumed abundance of carbon. As for more details about the mini CG method, see sections 4.1 and 6.3 of Paper II.

The above noted process is repeated blend-by-blend for all the EWs of CO measured in table 5. The resulting abundance corrections to the starting value of $\log A_C^{(0)} = -3.40$ for all the measured EWs given in table 5 are shown in figures 7a-g for our seven program stars. The mean abundance correction $\Delta \log A_C^{(1)}$ and the resulting carbon abundance $\log A_C^{(1)} = -3.40 + \Delta \log A_C^{(1)}$ are given in the fifth and sixth columns of table 6, respectively, for each object.

5.1.2. First iteration on the H_2O blends in region B

Since H_2O lines are sufficiently strong in region B (defined in figure 3 and detailed in section 3.4 of Paper II) for late M dwarfs, we first analyze the H_2O blends in region B listed in table 4 of Paper II. EWs measured by referring to the pseudo-continuum are given in table 7.

Given that the carbon abundance is now known to be $\log A_C^{(1)}$ from the analysis of CO in the preceding sub-

⁴ We use the notation: $A_{\text{El}} = N_{\text{El}}/N_{\text{H}}$, where N_{El} and N_{H} are the number density of the element El and hydrogen, respectively.

⁵ The CO abundance depends almost on the carbon abundance alone so far as $A_C < A_O$. However, this may no longer be true if $A_C \approx A_O$ and, to prevent such a circumstance when carbon alone is increased, we also changed oxygen abundance so that A_O/A_C ratio remains the same.

subsection, we apply the specified model for each object noted in the second column of table 8. Assuming an initial starting value of $\log A_{\text{O}}^{(0)} = \log A_{\text{C}}^{(1)} + 0.30$ ⁶, the mini CG is generated from the synthetic spectra for $\log A_{\text{O}}^{(0)}$ and $\log A_{\text{O}}^{(0)} \pm \delta$ ⁷ for each object. Since this starting value of oxygen may be fairly good as can be expected from our experience so far, we now apply the mini CG method with $\delta = 0.1$ instead of 0.3. The resulting oxygen abundance corrections $\Delta \log A_{\text{O}}^{(1)}$ are shown in figures 8a-g. The mean abundance correction $\Delta \log A_{\text{O}}^{(1)}$ and the resulting oxygen abundance $\log A_{\text{O}}^{(1)} = (\log A_{\text{C}}^{(1)} + 0.30) + \Delta \log A_{\text{O}}^{(1)}$ are given in the third and fourth columns of table 8, respectively, for each object.

5.1.3. Second iteration on the CO blends

Starting from $\log A_{\text{C}}^{(1)}$ and $\log A_{\text{O}}^{(1)}$ in tables 6 and 8, respectively, we proceed to the second iteration on the carbon abundance, using the specified model for each object noted in the seventh column of table 6. The resulting second carbon abundance corrections $\Delta \log A_{\text{C}}^{(2)}$ show more or less similar patterns as those in figures 7a-g. The second carbon abundance correction $\Delta \log A_{\text{C}}^{(2)}$, which is generally smaller than $\Delta \log A_{\text{C}}^{(1)}$, and the resulting carbon abundance $\log A_{\text{C}}^{(2)} = \log A_{\text{C}}^{(1)} + \Delta \log A_{\text{C}}^{(2)}$ are given in the eighth and ninth columns of table 6, respectively, for each object. Although we do not illustrate the results as in figures 7a-g, the decrease of the probable errors in the resulting abundances (compare columns 6 and 9 in table 6) confirms that the accuracy of the analysis is improved by the use of the better starting values in the second iteration.

5.1.4. Second iteration on the H₂O blends in region B

Starting from $\log A_{\text{C}}^{(2)}$ and $\log A_{\text{O}}^{(1)}$ in tables 6 and 8, respectively, second oxygen abundance corrections $\Delta \log A_{\text{O}}^{(2)}$ are obtained and the results also show more or less similar patterns as those of figures 8a-g. The second oxygen abundance correction $\Delta \log A_{\text{O}}^{(2)}$ and the resulting oxygen abundance $\log A_{\text{O}}^{(2)} = \log A_{\text{O}}^{(1)} + \Delta \log A_{\text{O}}^{(2)}$ are given in the fifth and sixth columns, respectively, of table 8 for each object.

5.1.5. Further Iteration on the H₂O blends in region A

From our experience in Paper II, we first thought that it is sufficient to analyze the H₂O blends only in region B for late M dwarfs. However, it appears that the H₂O lines in

region B are rather weak and noisy in the hottest object in our sample, GJ 873 (see figure 11a). Also, it appears that the spectrum of region B is disturbed by unknown cause in the coolest object LP 412-31 in our sample (see figure 11g). For these reasons, we decide to analyze the H₂O blends in region A (defined in figure 2 and detailed in section 3.3 of Paper II), where the H₂O lines are stronger. EWs are measured for the H₂O blends listed in table 2 of Paper II and the results are given in table 9.

We start from $\log A_{\text{C}}^{(2)}$ and $\log A_{\text{O}}^{(2)}$ in tables 6 and 8, respectively, and oxygen abundance corrections $\Delta \log A_{\text{O}}^{(3)}$ are obtained. The results are shown in figures 9a-g. The oxygen abundance correction $\Delta \log A_{\text{O}}^{(3)}$ and the resulting oxygen abundance $\log A_{\text{O}}^{(3)} = \log A_{\text{O}}^{(2)} + \Delta \log A_{\text{O}}^{(3)}$ are given in the third and fourth columns, respectively, of table 10 for each object. Note that the values of $\Delta \log A_{\text{O}}^{(3)}$ are generally less than the probable errors, and this fact confirms that the resulting oxygen abundances from region B are already well determined. However, the value of $\Delta \log A_{\text{O}}^{(3)}$ for GJ 873 is rather large compared with the probable error: This may be because the H₂O lines in region B are too weak in GJ 873 and hence their analysis cannot be accurate as noted above.

figure 7: p.17

figure 8: p.17

figure 9: p.18

table 5: p.30

table 6: p.30

table 7: p.31

table 8: p.31

table 9: p.32

table 10: p.32

5.2. Synthetic Spectra

5.2.1. CO 2-0 bandhead region

Based on $\log A_{\text{C}}^{(2)}$ and $\log A_{\text{O}}^{(2)}$ in tables 6 and 8, respectively, CO spectra near the 2-0 bandhead region are evaluated with the use of the specified models for our seven objects. The resulting predicted spectra, convolved with the slit function (Gaussian) of FWHM = 16 km s⁻¹, are compared with the observed ones in figures 10a-g. Note that the observed and predicted spectra are both normalized by their pseudo-continua.

The χ^2 value is evaluated from

$$\chi^2 = \frac{1}{N-1} \sum_{i=1}^N \left(\frac{f_{\text{obs}}^i - f_{\text{cal}}^i}{\sigma_i} \right)^2, \quad (2)$$

where f_{obs}^i and f_{cal}^i are observed and predicted spectra normalized by their pseudo-continua, respectively. N is the number of data points and σ_i is the noise level estimated from the S/N ratio in table 1 (assumed to be independent of i). The resulting χ^2 values are given in the last column of table 6. The χ^2 values are large for GJ 752B

⁶ If the starting value of $\log A_{\text{O}}^{(0)}$ is fixed to be the solar abundance as in the case of $\log A_{\text{C}}^{(0)}$, it is possible that $A_{\text{O}}^{(0)} \lesssim A_{\text{C}}^{(1)}$ depending on the analysis on carbon abundance in the preceding subsection. For this reason, we assume a more plausible starting oxygen abundance to be $A_{\text{O}}/A_{\text{C}} \approx 2$ as in the Sun (Allende Prieto et al. 2002).

⁷ The H₂O abundance depends not on the oxygen abundance, but on $A_{\text{O}} - A_{\text{C}}$. Then, unlike the case of CO in the preceding subsection, we fix the carbon abundance to be $\log A_{\text{C}}^{(1)}$ and only the oxygen abundance is changed to apply the mini CG method to the H₂O blends.

and GJ 1002, but the S/N ratios for these objects are also high (table 1, fifth column). Thus, it is to be noted that the χ^2 value is by no means a measure of goodness of the fit. The χ^2 value of LP 412-31 is also large even though the S/N ratio is not especially high. Inspection of figure 10g reveals that the fit is really poor in this case at the right edge (hatched region). The χ^2 value actually plays its expected role in this case, but this can more easily be known by the visual inspection of the plot.

5.2.2. H_2O in region B

Based on $\log A_C^{(2)}$ and $\log A_O^{(2)}$ in tables 6 and 8, respectively, H_2O spectra in a part of region B (about one fourth of region B) are evaluated with the use of the specified models given in the second column of table 8. The resulting predicted spectra are compared with the observed ones in figures 11a-g. The resulting χ^2 values are given in the last column of table 8. We again find the correlation of the χ^2 values with the S/N ratios of the observed spectra (region B is in the same echelle order as CO bands). The χ^2 value of LP 412-31 is again very large and this is due to unknown disturbance⁸ on the observed spectrum as seen on figure 11g (hatched region).

5.2.3. H_2O in region A

Based on $\log A_C^{(2)}$ and $\log A_O^{(3)}$ in tables 6 and 10 respectively, H_2O spectra in region A are computed with the use of the specified models for our seven objects. The resulting predicted spectra are compared with the observed ones in figures 12a-g. The χ^2 values for the fitting are given in the sixth column of table 10. The χ^2 values are large for GJ 752B, GJ 1002, and GAT 1370, and the S/N ratios for these objects are again high (table 1, fourth column). The χ^2 value for LP 412-31 is quite small, and this may reflect the very low S/N ratio on one hand and good overall fit without major defect in this region of the observed spectrum on the other.

figure 10: p.19

figure 11: p.20

figure 12: p.21

6. Rotational broadening

In the later M dwarfs, it is known that the fraction of the rapid rotators tends to be larger (e.g., Mohanty & Basri 2003; Jenkins et al. 2009). Our object 2MASS 1835+32 is also found to be a fast rotator: The projected rotational velocity of 2MASS 1835+32 was measured to be $44.0 \pm 4.0 \text{ km s}^{-1}$ (Reiners & Basri 2010) and $37.6 \pm 5.0 \text{ km s}^{-1}$ (Deshpande et al. 2012). We adopt the mean value of 40.8 km s^{-1} in the following analysis, and examine the effect of the uncertainty in the projected rotational velocity in section 7.4. So far, we neglected the rotational broad-

ening in our analysis of M dwarfs, since it can be negligible compared to the rather large instrumental broadening of our medium resolution spectrograph (FWHM $\approx 16 \text{ km s}^{-1}$). In the case of 2MASS 1835+32, the rotational broadening is much larger than the FWHM of the slit function, and we neglect it for simplicity in the following analysis.

We first examine the effect of rotation on the predicted spectrum in the bandhead region of CO 2-0 band. The molecular data used are the same as in Table 7⁹ of Paper I. The spectrum is first calculated for our dusty model Bc2280c526 assuming *case c* abundance, at the sampling interval of 0.02 \AA (resolution of $R \approx 10^{+5}$), and the result is shown by a thin line in figure 13a. This spectrum is convolved with the rotation profile $A(x)$ given by Unsöld (1955):

$$A(x) = \frac{\frac{2}{\pi}(1-x^2)^{\frac{1}{2}} + \frac{\beta}{2}(1-x^2)}{(1 + \frac{2}{3}\beta)} \quad (3)$$

with

$$x = \frac{\Delta \lambda}{b} \quad (4)$$

and

$$b = \frac{\lambda}{c} V_{\text{rot}} \sin i \quad (5)$$

where V_{rot} is the equatorial rotational velocity, and i is the angle between the rotation axis and the line of sight to the observer. Also, β is the limb-darkening coefficient defined by

$$I = \text{const}(1 + \beta \cos \theta) \quad (6)$$

where I is the intensity emerging at an angle θ with respect to the outward normal (we assume $\beta = 2/3$). The result convolved with the rotation profile of $V_{\text{rot}} \sin i = 40.8 \text{ km s}^{-1}$ is shown by a thick line in figure 13a.

For comparison, the same high resolution spectrum is convolved with the slit function (Gaussian) of FWHM = 16 km s^{-1} , and the result is shown in figure 13b. Comparison of figures 13a and 13b reveals that most CO blends with ref. nos. through 1 to 10 are smeared-out by the rotation and identities of these blends are lost. Only blends with ref. nos. 11 – 15 conserve their identities and we will use the blends of ref. nos 12 – 15 in our analysis of CO. The blend of ref. no. 11 is not used because the observed profile does not meet our criterion to accept a blend for our analysis (at least one wing reaches higher than the half of the line depth). It is to be noted that the pseudo-continuum level of the rotationally broadened spectrum (figure 13a) is lower than that of the broadened by the slit function of the spectrograph (figure 13b). In figure 13c, the observed spectrum of 2MASS 1835+32

⁸ Despite such a defect in a part of the observed spectrum, modest number of the H_2O blends to be used in the mini CG analysis can be measured (table 7) outside the region shown in figure 11g.

⁹ to which we add a blend with ref. no. 15. The spectroscopic data for the new blend are given in Appendix 1. The blend no. 15 was not used so far since this blend is mostly located at the edge of the 28th order of our echelle spectra. We use this blend in 2MASS 1835+32, since otherwise we have only three blends for our analysis and, fortunately, this blend is well observed in this object.

(dots) is compared with the rotationally broadened spectrum from figure 13a (thick line) after renormalized by the pseudo-continuum.

Next, we examine the effect of rotation on the H₂O spectrum. For this purpose, we select the region between 22510 and 22660 Å, a part of region B noted in Paper II (see its table 4). The high resolution spectrum is evaluated with the use of the line-list by BT2-HIGHTEMP2010 (Barber et al. 2006; Rothman et al. 2010) and the result is shown by a thin line in figure 14a. The result convolved with the rotational profile of $V_{\text{rot}} \sin i = 40.8 \text{ km s}^{-1}$ is shown by a thick line. For comparison, the same high resolution spectrum convolved with the slit function of $\text{FWHM} = 16 \text{ km s}^{-1}$ is shown in figure 14b on which the reference numbers introduced in Paper II are reproduced. Comparison of figures 14a and 14b reveals that the identities of some H₂O blends are conserved despite the rotational broadening and some blends appear at slightly shifted positions, including different components. We select eight features near B01, 02, 03, 04 07, 09, 12, and 14 for our mini CG analysis as indicated in figure 14c, where the observed spectrum of 2MASS 1835+32 (dots) is compared with the rotationally broadened spectrum of figure 14a (thick line).

But we could not analyze the H₂O blends in region A noted in Paper II (see its table 2), since it is difficult to define the pseudo-continuum level for highly depressed strong H₂O bands which are further smeared-out by rotation.

figure 13: p.22

figure 14: p.23

7. The M8.5 dwarf 2MASS J1835379+325954

In the M8.5 dwarf 2MASS 1832+35 in our sample, dust may form in its photosphere and this object is also known to be a rapid rotator. The analysis of the CO and H₂O spectra is done by the mini curve-of-growth method (subsection 7.1) and by the spectral synthesis method (subsection 7.2) as for the seven earlier M dwarfs, but we apply the dusty models (section 4.2) and consider the rotational broadening (section 6). The effects of dust (subsection 7.3), rotational velocity (subsection 7.4), and fundamental parameters (subsection 7.5) are examined. Based on the examinations of the various factors affecting the spectrum of 2MASS 1835+32, a best possible solution on the abundances and projected rotational velocity in this dusty rapid rotator is suggested (subsection 7.6).

7.1. Mini curve-of-growth analysis

We apply the fully dusty model of $T_{\text{eff}} = 2280 \text{ K}$, Bc2280c526, assuming $V_{\text{rot}} \sin i = 40.8 \text{ km s}^{-1}$ in our analysis of the CO and H₂O blends in this subsection throughout.

7.1.1. First iteration on the CO blends

We measure the equivalent widths of the CO blends with ref. nos. 12 - 15 on the observed spectrum by referring to the pseudo-continuum and the results are given in the ninth column of table 5. We again apply the mini CG method with the solar abundances of *case c* as initial starting values ($\log A_{\text{C}}^{(0)} = -3.61$ and $\log A_{\text{O}}^{(0)} = -3.31$), and determine the abundance corrections needed to explain the observed $\log W/\lambda$ values in table 5. The resulting abundance corrections for the four lines are shown in figure 15a and the mean value $\Delta \log A_{\text{C}}^{(1)} = -0.101$ is indicated by a dashed line. The resulting carbon abundance is $\log A_{\text{C}}^{(1)} = -3.711 \pm 0.128$ (table 11, line no. 1).

7.1.2. First iteration on the H₂O blends

We measure the equivalent widths of the H₂O blends near B01, 02, 03, 04 07, 09, 12, and 14 (see figure 14c) on the observed spectrum by referring to the pseudo-continuum and the results are given in the ninth column of table 7. We again apply the mini CG method to these blends. Since carbon abundance is now known to be $\log A_{\text{C}}^{(1)} = -3.711$, we estimate $\log A_{\text{O}}$ to be larger by 0.30 dex as in the Sun (Allende Prieto et al. 2002). Thus we start from $\log A_{\text{O}}^{(0)} = -3.711 + 0.30 = -3.411$ and since this value may be a good starting value, we now apply the mini CG method with $\delta = 0.1$. The resulting abundance corrections from the eight blends are shown in figure 16a and the mean value $\Delta \log A_{\text{O}}^{(1)} = +0.008$ is indicated by a dashed line. The result is $\log A_{\text{O}}^{(1)} = -3.403 \pm 0.024$ as given in table 11 (line no. 2).

7.1.3. Confirmation by second iteration

Given that we have now determined $\log A_{\text{C}}^{(1)}$ and $\log A_{\text{O}}^{(1)}$, we repeat the mini CG analysis with these values as starting values. Since the CO blends are contaminated with the weak H₂O lines, revised oxygen abundance may have some effect on the determination of carbon abundance from the CO blends. The resulting mean abundance corrections is only -0.025 (table 11, line no. 3), confirming that the first iteration is already close to the solution, and this may be because the oxygen abundance assumed in the first iteration is already close to the final result (as will be confirmed in table 11). With the revised carbon abundance, the H₂O blends are also examined and the resulting mean correction is only -0.012 (table 11, line no. 4).

We confirm that the first iteration is already near the convergence value. For this reason, we will skip the second iteration in the analysis to be given hereafter (subsections 7.3, 7.4, and 7.5), since these analyses are for comparison purpose to examine the effect of different assumptions. For consistency in these analyses, we will use the result of the first iteration given in table 11 (line nos. 1 and 2) as the reference.

figure 15: p.24

figure 16: p.24

table 11: p.33

7.2. Synthetic spectra

Based on the carbon and oxygen abundances given in table 11 (line nos. 1 and 2), synthetic spectra of CO and H₂O are computed and compared with the observed spectra in figures 17a and 18a, respectively. Although only four CO blends are used to obtain the carbon abundance from the CO spectrum, the whole CO spectrum including the bandhead region is reasonably well reproduced with the abundances based on the mini CG analysis. The χ^2 values for CO and H₂O are 5.803 and 2.035 (table 12, line no. 1), respectively ¹⁰.

figure 17: p.25

figure 18: p.26

table 12: p.33

7.3. Effect of dust on abundance determination

We apply our dusty model in our abundance analysis in subsections 7.1 and 7.2. We now examine the case of a dust-free model to assess the effect of dust in our analysis. For this purpose, we use the dust-free model of the same values of $T_{\text{eff}} = 2280$ K, $\log g = 5.26$, and $V_{\text{rot}} \sin i = 40.8 \text{ km s}^{-1}$ as the dusty model we applied in subsection 7.1. We assume the same initial abundances of $\log A_{\text{C}}^{(0)} = -3.61$ and $\log A_{\text{O}}^{(0)} = -3.31$, and apply the mini CG method to the CO blends as for the dusty model. The resulting abundance corrections are shown in figure 15b. The mean value of $\Delta \log A_{\text{C}}^{(1)} = -0.358 \pm 0.078$ is 0.257 dex smaller compared with the result of $\Delta \log A_{\text{C}}^{(1)} = -0.101 \pm 0.128$ using the dusty model.

Then, we assume the revised carbon abundance $\log A_{\text{C}}^{(1)} = -3.61 - 0.358 = -3.968$ and $\log A_{\text{O}}^{(0)} = -3.968 + 0.3 = -3.668$ as starting values, and analyze the H₂O blends. The resulting abundance corrections are shown in figure 16b and the mean value of $\Delta \log A_{\text{O}}^{(1)} = 0.144 \pm 0.034$ is compared with the result using the dusty model, $\Delta \log A_{\text{O}}^{(1)} = +0.008 \pm 0.024$. However, the starting values are different from those of the dusty case this time, and what is to be compared is the resulting $\log A_{\text{O}}^{(1)} = -3.668 + 0.144 = -3.524$ of the dust-free case with $\log A_{\text{O}}^{(1)} = -3.411 + 0.008 = -3.403$ of the dusty case. Summarizing, the carbon and oxygen abundances based on the dust-free model are $\log A_{\text{C}}^{(1)} = -3.968 \pm 0.078$ and $\log A_{\text{O}}^{(1)} = -3.524 \pm 0.034$ (table 11, line nos. 5 and 6), or smaller by 0.257 and 0.121 dex, respectively, compared with the case by the dusty model (table 11, line nos. 1 and 2).

We also compute the synthetic spectra of CO and H₂O, and the results are shown in figures 17b and 18b, respec-

tively. We also evaluate the χ^2 values which turn out to be $\chi^2(\text{CO}) = 10.369$ and $\chi^2(\text{H}_2\text{O}) = 2.879$ by the dust-free model (table 12, line no. 2), compared with $\chi^2(\text{CO}) = 5.803$ and $\chi^2(\text{H}_2\text{O}) = 2.035$ by the dusty model (table 12, line no. 1). Thus, the abundances based on the dusty model provide a better account of the observed spectra both of CO and H₂O. Also, the resulting carbon and oxygen abundances based on the dust-free model appear to be somewhat too small for an M dwarf of the disk population. For these reasons, we may conclude that the dusty model better represents the photospheric structure of 2MASS 1832+35 and that it is more appropriate for abundance analysis.

7.4. Effect of the rotational velocity

So far, we apply the projected rotational velocity of $V_{\text{rot}} \sin i = 40.8 \text{ km s}^{-1}$, which is a mean value of the two determinations by different groups (section 6). During our analysis, we notice that the projected rotational velocity has appreciable effect on the abundance determination. This is because the EWs are evaluated from the synthetic spectrum by referring to the pseudo-continuum level which depends on the rotational broadening, in our mini CG analysis. To examine the effect of the rotational velocity, we apply the mini CG method to the CO blends by assuming the lower value of $V_{\text{rot}} \sin i = 37.6 \text{ km s}^{-1}$ (Deshpande et al. 2012) and the higher value of $V_{\text{rot}} \sin i = 44.0 \text{ km s}^{-1}$ (Reiners & Basri 2010), both using the dusty model Bc2280c526 with the initial starting abundances of $\log A_{\text{C}}^{(0)} = -3.61$ and $\log A_{\text{O}}^{(0)} = -3.31$. The resulting abundance corrections are shown in figure 15c and 15d for the cases of the low and high rotational velocities, respectively. The resulting carbon abundances are $\log A_{\text{C}}^{(1)} = -3.794 \pm 0.094$ and -3.566 ± 0.199 (table 12, line nos. 7 and 9) for the low and high rotational velocities, respectively. Thus the difference of the resulting carbon abundances is 0.228 dex for the difference of $V_{\text{rot}} \sin i$ values by 6.4 km s^{-1} .

We also repeat the mini CG method for the H₂O blends and the results are shown in figures 16c and 16d for the cases of the low and high rotational velocities, respectively. The resulting oxygen abundances are $\log A_{\text{O}}^{(1)} = -3.461 \pm 0.036$ and -3.318 ± 0.029 (table 12, line nos. 8 and 10) for the cases of the low and high rotational velocities, respectively, and the difference is 0.143 dex for the difference of $V_{\text{rot}} \sin i$ values by 6.4 km s^{-1} .

The synthetic spectra of CO are shown in figures 17c and 17d for the cases of the low and high rotational velocities, respectively. The observed spectrum remains unchanged in figures 17c and 17d, but the pseudo-continuum level of the synthetic spectrum is lower ¹¹ in the case of the higher rotational velocity than in the case of the lower rotational velocity for the reason noted at the beginning of this subsection. For this reason, EWs of the CO blends

¹⁰ Although we notice in section 5.2 that the χ^2 values are not so useful as measures of the goodness of fits if applied to different objects having different S/N ratios, they are useful if applied to the same object analyzed by different models.

¹¹ The spectra in figures 17c and 17d are normalized already by the pseudo-continua. We confirm that the pseudo-continuum levels are 0.929 and 0.917 of the true continua in the low and high rotational velocities, respectively.

measured from the synthetic spectrum of the higher rotational velocity are smaller than those measured from the spectrum of the lower rotational velocity, as can directly be seen on figures 17c and 17d. Then, a higher abundance is required to explain the observed spectrum by the predicted spectrum based on the higher rotational velocity. The fitting appears to be better for the case of the higher rotational velocity for which the χ^2 value is 3.126 while it is 9.406 for the case of the lower rotational velocity (table 12, line nos. 3 and 4).

The similar analyses on the H_2O blends are shown in figures 16c and 16d for the cases of the low and high rotational velocities, respectively. The fittings appear to be somewhat better for the case of the higher rotational velocity, since the χ^2 values are 2.568 and 1.820 for the low and high rotational velocities, respectively (table 12, line nos. 3 and 4). By the way, $\chi^2(\text{CO}) = 5.803$ and $\chi^2(\text{H}_2\text{O}) = 2.035$ for the case of $V_{\text{rot}} \sin i = 40.8 \text{ km s}^{-1}$ discussed in subsection 7.2. In conclusion, the highest rotational velocity of $V_{\text{rot}} \sin i = 44.0 \text{ km s}^{-1}$ provides the best account of the observed spectra (compare line no. 1, 3, and 4 of table 12), and possibly the best carbon and oxygen abundances.

7.5. Effect of the fundamental parameters

Finally, we examine the effect of the uncertainty in the fundamental parameters, especially of T_{eff} by $\pm 100 \text{ K}$. For this purpose, we generate new dusty models of $T_{\text{eff}} = 2180$ and 2380 K . The gravities are estimated from the T_{eff} - radius - mass relations discussed in section 3. We apply our dusty models of the low and high values of T_{eff} , Bc2180cc528 and Bc2380c525, respectively, with the initial starting abundances of $\log A_{\text{C}}^{(0)} = -3.61$ and $\log A_{\text{O}}^{(0)} = -3.31$. We also assume $V_{\text{rot}} \sin i = 40.8 \text{ km s}^{-1}$. The resulting carbon abundance corrections by the mini CG analysis for the low and high T_{eff} models are shown in figures 15e and 15f, respectively. It appears that the resulting carbon abundance corrections are $\Delta \log A_{\text{C}}^{(1)} = +0.0003 \pm 0.136$ and -0.094 ± 0.142 (table 11, line nos. 11 and 13) for the low and high T_{eff} , respectively. For comparison, $\Delta \log A_{\text{C}}^{(1)} = -0.101 \pm 0.128$ for our adopted case of $T_{\text{eff}} = 2280 \text{ K}$ (table 11, line no. 1). Thus the changes of T_{eff} by $\pm 100 \text{ K}$ result in rather minor changes on the resulting carbon abundances. This should certainly be due to special circumstance noted in section 4.3 that the temperatures of the surface layers converge to the condensation lines of iron.

We repeat the same analysis on H_2O blends and the resulting abundance corrections are shown in figures 16e and 16f for the cases of the low and high T_{eff} , respectively. The resulting oxygen abundances are $\log A_{\text{O}}^{(1)} = -3.324 \pm 0.023$ and -3.388 ± 0.023 (table 11, line nos. 12 and 14) for $T_{\text{eff}} = 2180$ and 2380 K , respectively. For comparison, $\log A_{\text{O}}^{(1)} = -3.403 \pm 0.024$ for $T_{\text{eff}} = 2280 \text{ K}$ (table 11, line no. 2). Again, the oxygen abundance depends little on T_{eff} . This is a favorable result, since the effective temperature is difficult to determine in very cool M dwarfs since no angular diameter measurement is available yet.

We then compute the synthetic spectra of CO for the

abundances determined for the cases of the low and high T_{eff} and the results are shown in figures 17e and 17f, respectively. We also compute the synthetic spectra of H_2O for the abundances determined for the cases of the low and high T_{eff} and the results are shown in figures 18e and 18f, respectively. The results are again not much different compared with the reference case, and the χ^2 values are nearly the same for three cases (compare line nos. 1, 5, and 6 of table 12).

7.6. Carbon and oxygen abundances in 2MASS 1835+32

In the latest M dwarf 2MASS 1835+32 in our sample, the dust formation and rapid rotation introduce additional uncertainty in the abundance determinations. The effect of the dust formation is appreciable (subsection 7.3), but this is based on the simplest assumption on the dust formation based on the thermodynamics alone. The limitation of such a simple approach will be discussed in section 8.2, but we think that even our simple treatment of dust provides a better account of the observed spectrum of 2MASS 1835+32 compared with the case based on the dust-free model, and we decide to apply our dusty models in our abundance analysis of this object.

The effect of the rotational velocity turns out to be unexpectedly large. We first apply the mean value ($V_{\text{rot}} \sin i = 40.8 \text{ km s}^{-1}$) of the two available values in the literature (section 6), but we find that the higher value ($V_{\text{rot}} \sin i = 44.0 \text{ km s}^{-1}$) of the two literature values gives the better account of the observed spectrum (subsection 7.4). The empirical determinations of the rotational velocity are anyhow difficult in late M dwarfs since the true-continuum level of the observed spectrum cannot be well defined in general and, further, abundances and physical parameters (or model photosphere applied) must be properly assigned. We believe that our analysis can be a way to clear these requirements. Since our analysis suggests a higher value of the known $V_{\text{rot}} \sin i$ values, we examine a still higher value of $V_{\text{rot}} \sin i = 48.0 \text{ km s}^{-1}$ and repeat the analysis outlined in subsection 7.4. The results are $\log A_{\text{C}} = -3.451 \pm 0.298$ and $\log A_{\text{O}} = -3.245 \pm 0.044$. However, we can use only four lines of CO, and we notice that the internal consistency (p.e.) of our CO analysis turns out to be worse for the higher $V_{\text{rot}} \sin i$ value. Also we find that $\chi^2 = 3.476$ for the comparison of the observed and predicted spectra of CO, and $V_{\text{rot}} \sin i = 48.0 \text{ km s}^{-1}$ does not provide any improvement over the result based on 44.0 km s^{-1} for which $\chi^2 = 3.126$ (table 12, lone no. 4).

The abundances of $\log A_{\text{C}} = -3.711$ and $\log A_{\text{O}} = -3.403$ based on $V_{\text{rot}} \sin i = 40.8 \text{ km s}^{-1}$ (table 11, line nos. 1 and 2) are somewhat too low for a possibly young object like 2MASS 1835+32 which is not spun down yet. On the other hand, the abundances of $\log A_{\text{C}} = -3.566$ and $\log A_{\text{O}} = -3.318$ based on $V_{\text{rot}} \sin i = 44.0 \text{ km s}^{-1}$ (table 11, line nos. 9 and 10) appear to be acceptable for 2MASS 1835+32 which may be a relatively young M dwarf as noted above. Also, inspection of table 12 reveals that this case provides the best account of the observed spectrum among the six possible cases we have examined. For these reasons, we adopt $\log A_{\text{C}} = -3.57 \pm 0.20$ and

$\log A_O = -3.32 \pm 0.03$ together with $V_{\text{rot}} \sin i = 44.0 \text{ km s}^{-1}$ for 2MASS 1835+32 (table 13).

8. Discussion

8.1. Carbon and oxygen abundances in M dwarfs

We take the weighted mean (with the numbers of lines used as weights) of the oxygen abundances resulting from the analyses of regions A (table 10) and B (table 8) for the seven M dwarfs for which the two regions have been analyzed. The results and that from region B alone (2MASS 1835+32) are summarized in table 13 together with the carbon abundances from tables 6 and 11 (line nos. 9 and 10). Also, the classical and more recent solar carbon and oxygen abundances by Anders & Grevesse (1989) and Asplund et al. (2009), respectively, are included in table 13 for comparison.

The resulting values of $\log A_O/A_C$ (given in the fourth column of table 13) are plotted against the values of $\log A_C$ in figure 19 by red (or black) filled circles. The results for 38 M dwarfs analyzed in Papers I & II are reproduced from figure 15 of Paper II, as shown by green (or grey) filled circles. The two representative solar values are shown by \odot marks. Inspection of figure 19 reveals that the late M dwarfs show no systematic difference from the early and middle M dwarfs, and our conclusion outlined in Paper II that the A_O/A_C ratios are larger at the lower metallicities and gradually decrease in the higher metallicities is strengthened with the additional data on the eight late M dwarfs.

Although the large production of oxygen in the metal-poor era is explained as due to Type II supernovae/hypernovae in the early Galaxy (Nomoto et al. 2013), the large differential effect in the productions of carbon and oxygen is by no means well understood (Gustafsson et al. 1999), and accurate determinations of the carbon and oxygen abundances will still be needed. Especially, our analysis is limited to the M dwarfs in the disk, and to extend our analysis to the halo M dwarfs (M subdwarfs) is a next major step. However, besides the observational difficulty to observe faint M subdwarfs, the K band region of the metal deficient M dwarfs is badly depressed by the strong collision-induced absorption (CIA) due to $\text{H}_2 - \text{H}_2$ and $\text{H}_2 - \text{He}$ pairs (Borysow et al. 1997). In fact, the CO and H_2O bands we have analyzed in our present work are almost unseen on the observed spectra of a few late M subdwarfs, at least by low resolutions (Burgasser & Kirkpatrick 2006). For this reason, abundance analysis of M subdwarfs will be quite challenging even if higher resolution spectra of M subdwarfs can be obtained by future large telescopes.

By the way, the effect of H_2 CIA on the abundance analysis is by no means well evaluated so far as we are aware, and we examine this problem in the case of a relatively cool M dwarf GJ 752B as an example. In figure 20, we plot the predicted spectrum of CO based on our model of GJ 752B (Cc2640c526) but disregarding the H_2 CIA due to $\text{H}_2 - \text{H}_2$ and $\text{H}_2 - \text{He}$ pairs (blue/black solid line), and

compare it with that based on the same model but including the H_2 CIA (light sky/grey solid line) as we have done so far (i.e., the same as figure 10f). The resulting CO spectrum computed disregarding the H_2 CIA is stronger than that including the H_2 CIA, as expected. Then, we apply the mini CG analysis based on our model of GJ 752B but disregarding the H_2 CIA to the CO lines, and determine the abundance correction to the $\log A_C$ based on the model including the H_2 CIA ($\log A_C = -3.550 \pm 0.066$, see Table 6). The result is $\Delta \log A_C = -0.196 \pm 0.081$ as shown in figure 21, and the effect of neglecting the H_2 CIA is to reduce the logarithmic carbon abundance by 0.196 dex. Thus, the effect of the H_2 CIA is appreciable even in the solar metallicity case, even if it is not so drastic as in the metal-poor cases (Borysow et al. 1997).

figure 19: p.27

figure 20: p.27

figure 21: p.28

table 13: p.34

8.2. Dust in the photospheres of M dwarfs

In section 4.2, we assume that dust forms everywhere in the photospheres of M dwarfs so long as the thermochemical condition for condensation is fulfilled. However, it is now known that dust does not fill in the whole photosphere where thermochemical condition of condensation is fulfilled, at least in L and T dwarfs. In fact, if dust forms this way, more dust should be formed in the cooler dwarfs, and hence the cooler dwarfs should increasingly be red. However, observations never follow such an expectation. For example, $J - K$ color first shows reddening from late M to L dwarfs, but it turns to blue after late L dwarfs (e.g., Knapp et al. 2004), suggesting that dust in the photospheres should decrease towards late T dwarfs.

We have developed a simple model referred to as the unified cloudy model, UCM (Tsuji 2002): Dust grains first form at T_{cond} , the condensation temperature, but dust grains grow larger at cooler temperature and will precipitate at a certain temperature which we referred to as the critical temperature, T_{cr} . Then, dust grains exist only in the limited region of $T_{\text{cr}} \lesssim T \lesssim T_{\text{cond}}$ or dust grains appear in a form of cloud. In an L dwarf, T_{eff} (approximately the temperature where optical depth is about unity) is sufficiently higher than T_{cond} (see figure 5) as well as T_{cr} (1700, 1800, 1900 K and T_{cond}). For this reason, the dust cloud appears in the optically thin region and the L dwarf appears dusty. On the other hand, T_{eff} of a T dwarf is generally lower than T_{cond} as well as T_{cr} , and the dust cloud is situated in the optically thick region. For this reason, the dust cloud will have little observable effect and the T dwarf appears observationally as if it is dust-free. Then, observed characteristics of the spectra of L and T dwarfs could naturally be accounted for as a single sequence of T_{eff} in our UCMs.

However, further progress in photometry of L and T dwarfs revealed that the infrared colors such as $J - K$

(Knapp et al. 2004) show a large variation at a given effective temperature (Vrba et al. 2004). This fact suggests that the infrared colors are not determined by the T_{eff} alone, and we proposed that the critical temperature, T_{cr} , introduced in our UCMs, should be changing at a given T_{eff} (Tsuji 2005). Since the value of T_{cr} essentially defines the thickness of the dust cloud¹², we concluded that the thickness of the dust cloud should be changing at a fixed T_{eff} . Further, the change of the spectra from L6.5 to T3.5, for example, could be explained as a result of increasing T_{cr} from 1700 K to T_{cond} while T_{eff} remains nearly constant at $T_{\text{eff}} \approx 1300$ K (see Fig.10 of Tsuji 2005). This fact implies that the spectra as well as infrared colors of L and T dwarfs are not determined primarily by T_{eff} but should be determined by T_{cr} or the thickness of the dust cloud. Given that dust has such large and definitive effect on the observed spectra and colors, the values of T_{cr} can be inferred from observations in L and T dwarfs.

Although our cloudy models could be applied to L and T dwarfs, we are not sure if the same cloudy models can be applied to late M dwarfs. In fact, we have no means by which to estimate the value of T_{cr} in the case of M dwarfs, since the effect of dust on the observed spectra is rather subtle compared with that in L and T dwarfs. For this reason, we do not apply the cloudy models included in our UCMs to M dwarfs, but apply the simple fully dusty models of case B, also included as a subset in our UCM grid. If dust grains form a thin cloud in M dwarfs, our treatment provides a maximum estimate of the effect of dust.

Such a limitation of our simple approach basically based on the thermodynamics alone has been overcome by the recent development of the self-consistent treatment of dust formation coupled with the photospheric structure (Helling et al. 2008b; 2008c). These authors followed the kinematic processes of nucleation, dust growth, and evaporation, resulting in gravitational settling in the atmosphere, and the resulting dust cloud structure was incorporated into the photospheric model structure. They have applied their method to the substellar atmospheres for a wide range of metallicity extending to $[M/H]$ as low as -6.0 and showed that dust clouds form even in the most metal-poor substellar objects (Witte et al. 2009). They also have applied their method to evaluate the synthetic spectra of cool dusty dwarfs including late M dwarfs, and showed that the observed infrared spectra of late M and L dwarfs could be well fitted with their model predictions (Witte et al., 2011). Such a success is quite encouraging for the spectral analysis of dusty dwarfs, and we hope that their method will be extended to the abundance analysis on high resolution spectra of the dusty M dwarfs and subdwarfs in the near future.

One important effect of dust formation on abundance analysis is the element depletion by dust grains. We examine this problem within the framework of our LTE model

and estimate the effect of dust formation on the abundance determination in our case of 2MASS 1825+32 based on the photospheric model Bc2280c526. For this purpose, we plot in figure 22 the logarithm of the fraction f_{mol} of oxygen atoms in the species (including molecules and dust grains formed in the photosphere) defined by

$$f_{\text{mol}} = q P_{\text{mol}} / P(\text{O}), \quad (7)$$

where P_{mol} ¹³ is the partial pressure of a molecule and q is the number of oxygen atoms in the chemical formula of the molecule. Also, $P(\text{O})$ is the fictitious pressure of oxygen nuclei

$$P(\text{O}) = A_{\text{O}} P(\text{H}), \quad (8)$$

with the fictitious pressure of hydrogen nuclei $P(\text{H})$ obtained from

$$P(\text{H}) = P_{\text{H}^+} + P_{\text{H}} + 2P_{\text{H}_2}, \quad (9)$$

where P_{H^+} , P_{H} , and P_{H_2} are the partial pressures of H^+ , H , and H_2 , respectively, in the photosphere.

Inspection of figure 22 reveals that oxygen atoms are mostly depleted by CO , H_2O , and SiO . We consider only three dust species (corundum, iron, and enstatite), and the dust grain that works as a sink of oxygen is only corundum (Al_2O_3), since enstatite (MgSiO_3) does not form in our dusty model yet (see figure 5). In the abundance analysis based on H_2O , the fraction of oxygen that is depleted by corundum must be corrected for, but we skipped this correction since the corundum consumes only about 1% of oxygen and hence its effect on the oxygen abundance is about 1%. If enstatite forms, its effect on the oxygen abundance should be larger, since Si and Mg consume more than 10% of oxygen because of their higher abundance (about 10% of the oxygen abundance). For this reason, we are considering enstatite as a sink of oxygen in our chemical equilibrium, but this effect is not shown in figure 22, since enstatite does not form in our model of the late M dwarf 2MASS 1835+32 (see figure 5). Then, the uncertainty in our oxygen abundance due to dust formation may be about 1% within the framework of our present LTE analysis. Certainly, the dust species considered by us are limited (only three) and the effect of element depletion should be different if more dust species are considered (Helling et al. 2008c). But the amount of the oxygen depletion, for example, is limited by the abundances of non-volatile elements (Al, Mg, Si, etc.) that combine with oxygen and we hope that an approximate effect of dust formation on abundance analysis can be represented by the species that consumes the larger amount of oxygen atoms (e.g. corundum in our case discussed above under the absence of enstatite). However, it is certainly necessary to consider more dust species if higher accuracy in abundance determination is required.

figure 22: p.28

¹² In our UCM, dust cloud is located in the regime of $T_{\text{cr}} \lesssim T \lesssim T_{\text{cond}}$, where T_{cond} is uniquely determined by thermodynamics while T_{cr} is a free parameter to be fixed empirically. Then, thickness of the dust cloud is larger if the difference of T_{cr} against T_{cond} is larger.

¹³ For a solid particle such as corundum, for example, $P_{\text{Al}_2\text{O}_3}$ is the fictitious pressure of the monomer Al_2O_3 that would appear when corundum is fully dissolved into its constituent monomers.

8.3. The end of the main sequence

Probably, our present sample includes some objects near the end of the main sequence. The latest ones, such as GAT 1370, LP 412-31, and 2MASS 1835+32 are even referred to as brown dwarfs in SIMBAD, but the reason for these assignments is by no means clear for us. Unfortunately, we do not know how to exactly discriminate a brown dwarf from a star for a particular object in question. This is because there is no definite spectral criterion by which to identify the substellar nature. The Li test (Robolo et al. 1992) applied to field objects is effective in confirming the brown dwarf status of objects less massive than $0.06 M_{\odot}$, while the three objects mentioned above are likely to be more massive than $0.06 M_{\odot}$ (table 3). This method requires reasonably high spectral resolution and may be difficult to be used as a spectroscopic criterion in spectral classification level. Spectral classification of late M dwarfs, however, is also hampered by the presence of dust in their photospheres. Unlike atomic and molecular lines that show definitive signatures of their origins, dust spectra have no such signature. For this reason, it is not yet known how the effect of dust can be taken into account into the spectral classification of late M dwarfs. Anyhow, it is difficult to define the end of the main-sequence observationally and we simply follow the spectral classification that has classified our objects as M dwarfs in the present work.

On the other hand, the observed HR diagram at the end of the main sequence is well explained by the evolutionary model by Baraffe et al. (1998) (section 6.4 of Paper I) and consistent with their theoretical HR diagram (see figure 17 in Paper I). Also, some physical parameters predicted by their model are well consistent with the observed values (figures 2 - 4). For this reason, our estimations of some physical parameters are helped by their evolutionary model (section 3). Also, chemical abundances are shown to be rather normal down to the end of the main sequence, even though our analysis has been limited to the carbon and oxygen abundances yet, and our result appears to be consistent with the present idea of the Galactic chemical evolution (e.g., figure 19).

9. Concluding remarks

Our spectroscopic analysis of M dwarfs is greatly helped by the recent progress in observations, including the angular diameter measurements by the interferometry (e.g., Boyajian et al. 2012), infrared spectroscopy using new detectors (e.g., Kobayashi et al. 2000), and high precision astrometry (e.g., van Leeuwen 2007) and photometry (e.g., Wright et al. 2010) from space. A remaining problem in the present paper is that the effective temperatures of the latest M dwarfs cannot be determined by directly measured angular diameters, and we hope that the angular diameter measurements can be extended to late M dwarfs in the near future.

We have determined the carbon and oxygen abundances in $38 + 8 = 46$ M dwarfs from the CO and H₂O spectra

through our Papers I, II, and III, and the carbon abundances in additional four early M dwarfs in Paper I. So far, M dwarfs might not be expected to be proper objects for abundance determinations in general, but we now believe that such a prejudice should be reconsidered. In fact, we think that the stellar carbon and oxygen abundances can best be determined from the numerous CO and H₂O lines, respectively, observed in the spectra of M dwarfs, especially because stable CO and H₂O molecules are the major species of carbon and oxygen, respectively, in M dwarfs and hence their abundances are almost unaffected by the uncertainty in photospheric structures (Paper II). For this reason, the resulting carbon and oxygen abundances are insensitive to the imperfect model photospheres used in the abundance analysis. This fact shows a marked contrast to the well known difficulties in determining carbon and oxygen abundances from other molecular or atomic lines usually pretty model-sensitive in solar-type stars. An example of such an advantage is that the atypical nature of the recently revised solar carbon and oxygen abundances (Asplund et al. 2009) for its metallicity, compared with the nearby unevolved stars, has been demonstrated clearly by our analysis (see figure 15 of Paper I and figure 16 of Paper II for C and O, respectively), because of the higher internal consistency of our analysis based on M dwarfs compared with the other works based on the solar-type stars.

Also, even though the true-continuum cannot be seen in the spectra of M dwarfs, the pseudo-continuum defined by numerous lines of H₂O can be well defined observationally and, at the same time, it can theoretically be evaluated fairly accurately thanks to the recent high precision line list of H₂O (e.g., Barber et al. 2006; Rothman et al. 2010). Then, the basic principle of the quantitative analysis of the stellar spectra can be applied essentially in the same way without regard to whether the true- or the pseudo-continuum is referred to. This way, the difficulty of the continuum in cool stars is resolved at least in the near infrared spectra of M dwarfs (Paper I). Also, our analysis is not necessarily limited to the well defined unblended lines but can be extended to any blends by the use of a flexible method such as the mini curve-of-growth analysis.

In late M dwarfs, dust formation and rotation introduce additional problems in the spectroscopic analysis. Especially, effect of dust on abundance analysis involves complicated problems such as cloud formation, element depletion by dust grains, dust properties and so on, and impressive progress is being achieved in this field (section 8.2). In the present paper, however, we have restricted our analysis to a simple treatment based on the thermodynamical argument, and we hope that the effect of dust formation on abundance determination can be estimated approximately. Except for the dusty M dwarfs, CO and H₂O remain as excellent abundance indicators of carbon and oxygen, respectively, even in late M dwarfs (Paper III).

What we have done in our present work, however, is limited to the carbon and oxygen abundances determined

from the CO and H₂O spectra, respectively, and it is true that this is due to some favorable conditions in these particular cases. It is still to be investigated if similar analysis can be extended to other molecular or atomic spectra, but it is by no means trivial if such an extension can be done easily. However, given the recent progress in observations and in basic data such as molecular data, we believe that stellar spectroscopy will have great possibility in uncovering abundant information coded in high resolution stellar spectra.

We thank an anonymous referee for careful reading of our text and for helpful suggestions, especially on the cloud formation in dusty M dwarfs.

We thank the staff of the Subaru Telescope and S. Sorahana for the help with observations.

This research makes use of data products from the Wide-field Infrared Survey Explorer which is a joint project of the University of California, Los Angeles, and the Jet Propulsion Laboratory/California Institute of Technology, funded by NASA.

This research has made use of the VizieR catalog access tool and the SIMBAD database, both operated at CDS, Strasbourg, France, and of the RECONS database in www.recons.org.

Computations are carried out on common use data analysis computer system at the Astronomy Data Center, ADC, of the National Astronomical Observatory of Japan.

Appendix 1. Additional spectroscopic data of CO lines (2-0 band)

In addition to the CO blends referred to as nos. 1 - 14 in table 7 of Paper I, we use an additional blend referred to as no. 15 in this paper and the spectroscopic data for this blend composed of two CO lines are given in table 14.

table 14: p.34

References

- Allende Prieto, C., Lambert, D. L., & Asplund, M. 2002, *ApJ*, 573, L137
- Anders, E., & Grevesse, N. 1989, *Geochim. Cosmochim. Acta*, 53, 197
- Asplund, M., Grevesse, N., Sauval, A. J., & Scott, P. 2009, *ARA&A*, 47, 481
- Baraffe, I., Chabrier, G., Allard, F., & Hauschildt, P. H. 1998, *A&A*, 337, 403
- Barber, R. J., Tennyson, J., Harris, G. J., & Tolchenov, R. N. 2006, *MNRAS*, 368, 1087
- Becklin, E. E., & Zuckerman, B. 1988, *Nature*, 336, 656
- Borysow, A., Jørgensen, U. G., & Zheng, C. 1997, *A&A*, 324, 185
- Boyajian, T. S., et al. 2012, *ApJ*, 757, 112
- Burgasser, A. J., & Kirkpatrick, J. D. 2006, *ApJ*, 645, 1485
- Delfosse, X., Forveille, T., Ségransam, D., Beuzit, J.-L., Udry, S., Perrier, C., & Mayor, M. 2000, *A&A*, 364, 217
- Deshpande, R., et al. 2012, *AJ*, 144, 99
- Epchtein, N., et al. 1999, *A&A*, 349, 236
- Gliese, W., & Jahreiss, H. 1991, Preliminary Version of the Third Catalogue of Nearby Stars (Greenbelt: NASA/Astronomical Data Center)
- Gustafsson, B., Karlsson, T., Olsson, E., Edvardsson, B., & Ryde, N. 1999, *A&A*, 342, 426
- Hayashi, C., & Nakano, T. 1963, *Prog. Theor. Phys.*, 30, 460
- Helling, Ch., et al. 2008a, *MNRAS*, 391, 1854
- Helling, Ch., Dehn, M., Woitke, P., & Hauschildt, P. H. 2008b, *ApJ*, 675, L105
- Helling, Ch., Woitke, P., & Thi, W.-F. 2008c, *A&A*, 485, 547
- Helling, Ch., & Casewell, S. 2014, *A&A Rev.*, 22, 80
- Heney L., Vardya, M. S., & Bodenheimer, P. 1965, *ApJ*, 142, 841
- Jones, H. R. A., & Tsuji, T. 1997, *ApJ*, 480, L39
- Joy, A. H., & Abt, H. A. 1974, *ApJS*, 28, 1
- Jenkins, J. S., Ramsey, L. W., Jones, H. R. A., Pavlenko, Y., Gallardo, J., Barnes, J. R., & Pinfield, D. J. 2009, *ApJ*, 704, 975
- Kirkpatrick, J. D., et al. 1999, *ApJ*, 519, 802
- Knapp, G. R., et al. 2004, *AJ*, 127, 3553
- Kobayashi, N., et al. 2000, *Proc. SPIE*, 4008, 1056
- Kumar, S. S. 1963, *ApJ*, 137, 1121
- Lawrence, A., et al. 2007, *MNRAS*, 379, 1599
- Leggett, S. K. 1992, *ApJS*, 82, 351
- Marley, M. S. & Robinson, T. D. 2015, *ARA&A*, 53, 279
- Mohanty, S., & Basri, G. 2003, *ApJ*, 583, 451
- Nakajima, T., Oppenheimer, B. R., Kulkarni, S. R., Golimowski, D. A., Matthews, K., & Durrance, S. T. 1995, *Nature*, 378, 463
- Nomoto, K., Kobayashi, C., & Tominaga, N. 2013, *ARA&A*, 51, 457
- Oppenheimer, B. R., Kulkarni, S. R., Matthews, K., & Nakajima, T. 1995, *Science*, 270, 1478
- Reid, I. N., et al. 2003, *AJ*, 125, 354
- Reiners, A., & Basri, G. 2010, *ApJ*, 710, 924
- Robolo, R., Martin, E. L., & Magazzù, A. 1992, *ApJ*, 389, L83
- Rothman, L. S., et al. 2010, *JQSRT*, 111, 2139
- Skrutskie, M. F., et al. 2006, *AJ*, 131, 1163
- Smith, V. V., et al. 2003, *ApJ*, 599, L107
- Tsuji, T. 1965, *PASJ*, 17, 152
- Tsuji, T. 1966, in *Proceedings of the Colloquium on Late-Type Stars* ed. M. Hack (Trieste: Osservatorio Astronomico di Trieste), 260
- Tsuji, T. 2002, *ApJ*, 575, 264
- Tsuji, T. 2005, *ApJ*, 621, 1033
- Tsuji, T., & Nakajima, T. 2014, *PASJ*, 66, 98 (Paper I)
- Tsuji, T., Nakajima, T., & Takeda, Y. 2015, *PASJ*, 67, 26 (Paper II)
- Tsuji, T., Ohnaka, K., & Aoki, W. 1996a, *A&A*, 305, L1
- Tsuji, T., Ohnaka, K., Aoki, W., & Nakajima, T. 1996b, *A&A*, 308, L29
- Unsöld, A. 1955, *Physik der Sternatmosphären mit Besonderer Berücksichtigung der Sonne*, 2ten Auf., (Berlin: Springer-Verlag), 509
- van Leeuwen, F. 2007, *A&A*, 474, 653
- Vrba, F. J., et al. 2004, *AJ*, 127, 2948
- Witte, S., Helling, Ch., & Hauschildt, P. H. 2009, *A&A*, 506, 1367
- Witte, S., Helling, Ch., Barman, T., Heidrich, N., & Hauschildt, P. H. 2011, *A&A*, 529, A44
- Wright, E. L., et al. 2010, *AJ*, 140, 1868
- York, D. G., et al. 2000, *AJ*, 120, 1579

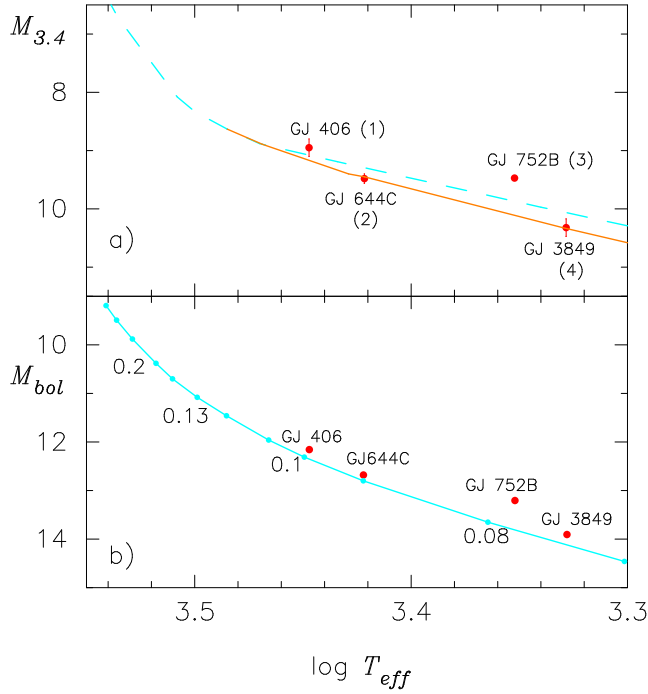


Fig. 1. a) The absolute magnitude at $3.4 \mu\text{m}$, $M_{3.4}$, plotted against $\log T_{\text{eff}}$ for four late M dwarfs, where T_{eff} values are based on the infrared flux method and a dashed line is a mean curve from figure 1 of Paper I. b) The absolute bolometric magnitude, M_{bol} , plotted against $\log T_{\text{eff}}$ for the four late M dwarfs in a) and a solid line (some numbers on it are the values of stellar mass M/M_{\odot}) is the theoretical HR diagram by Baraffe et al. (1998), reproduced from figure 17 of Paper I. It is to be noted that the positions of three objects GJ 406, GJ 644C, and GJ 3849 are consistent with the theoretical HR diagram. For this reason, we apply these three objects to revise the $M_{3.4} - \log T_{\text{eff}}$ relation for late M dwarfs and we propose a slightly modified $M_{3.4} - \log T_{\text{eff}}$ relation shown by a solid line in a).

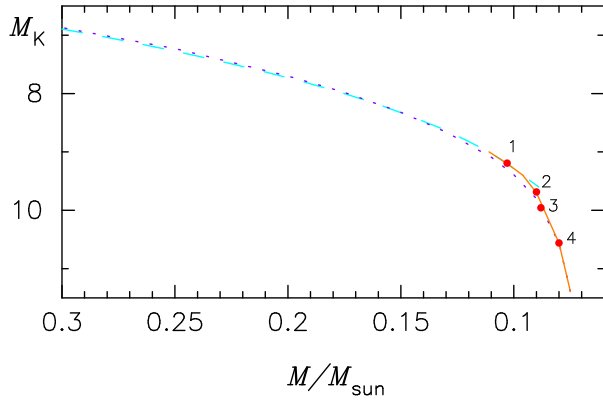


Fig. 2. Mass-luminosity (M_K) relation by Delfosse et al. (2000) (dashed line) is extended to late M dwarfs using that based on the evolutionary models by Baraffe et al. (1998) (dotted line). The masses of the calibration stars in table 4 are obtained from the resulting mass-luminosity relation shown by a solid line.

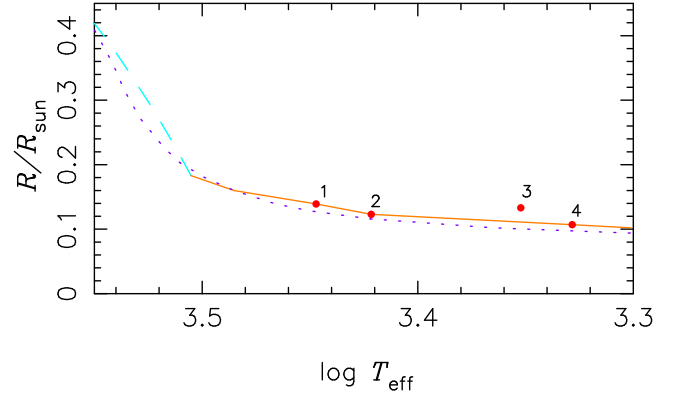


Fig. 3. $R/R_{\odot} - \log T_{\text{eff}}$ relation by equation 8 of Boyajian et al. (2012) (dashed line) is extended to late M dwarfs (solid line) based on our calibration stars no. 1, 2, & 4 in table 4. The theoretical relation based on the evolutionary models by Baraffe et al. (1998) is shown by a dotted line.

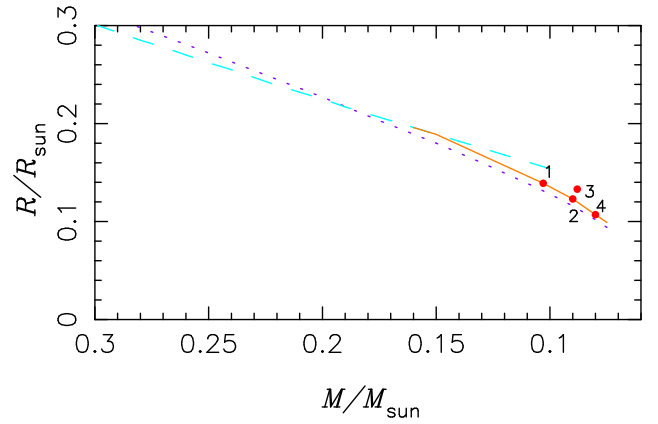


Fig. 4. $R/R_{\odot} - M/M_{\odot}$ relation by equation 10 of Boyajian et al. (2012) (dashed line) extended to late M dwarfs (solid line) based on the calibration stars no. 1, 2, & 4 in table 4. A dotted line is based on the evolutionary model by Baraffe et al. (1998).

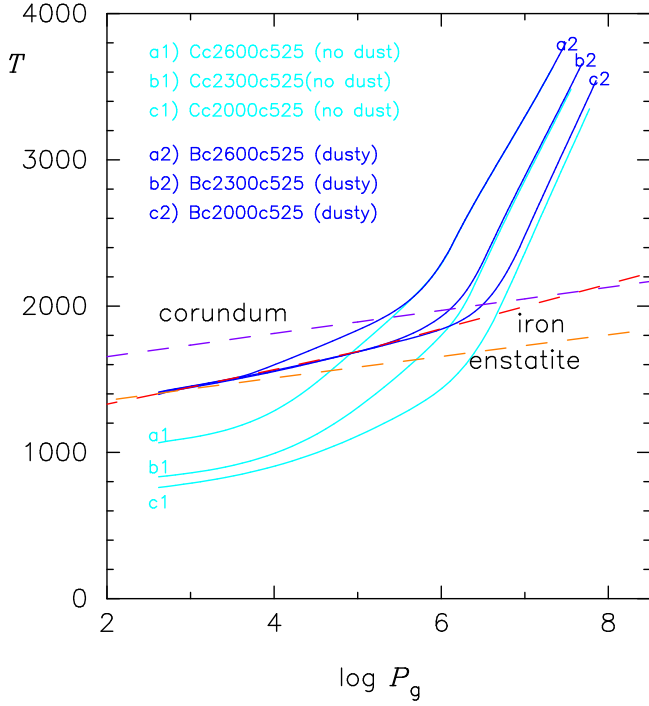


Fig. 5. Thermal structures of the dusty (curves a2, b2, and c2 shown by blue or black lines) and dust-free (curves a1, b1, and c1 shown by light sky or grey lines) models are compared for $T_{\text{eff}} = 2600, 2300$, and 2000 K (*case c*, $\log g = 5.25$). The condensation temperatures of corundum, iron, and enstatite are shown by dashed lines.

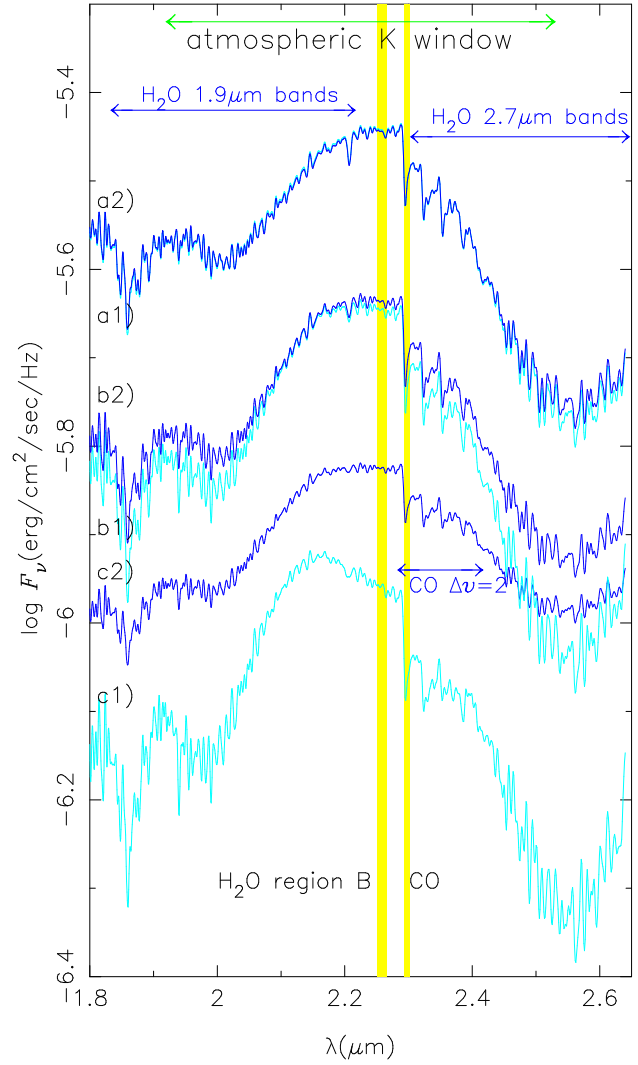


Fig. 6. Theoretical spectra ($R = 600$) of the dusty (curves a2, b2, and c2 shown by blue or black lines) and dust-free (curves a1, b1, and c1 shown by light sky or grey lines) models are compared for $T_{\text{eff}} = 2600, 2300$, and 2000 K (*case c*, $\log g = 5.25$). The effect of dust on the spectra is still negligible for $T_{\text{eff}} = 2600$, noticeable for $T_{\text{eff}} = 2300$, and quite large for $T_{\text{eff}} = 2000$. The regions indicated by CO and H₂O region B (shown by yellow or grey) are selected for detailed analysis of CO and H₂O lines in 2MASS 1835+32.

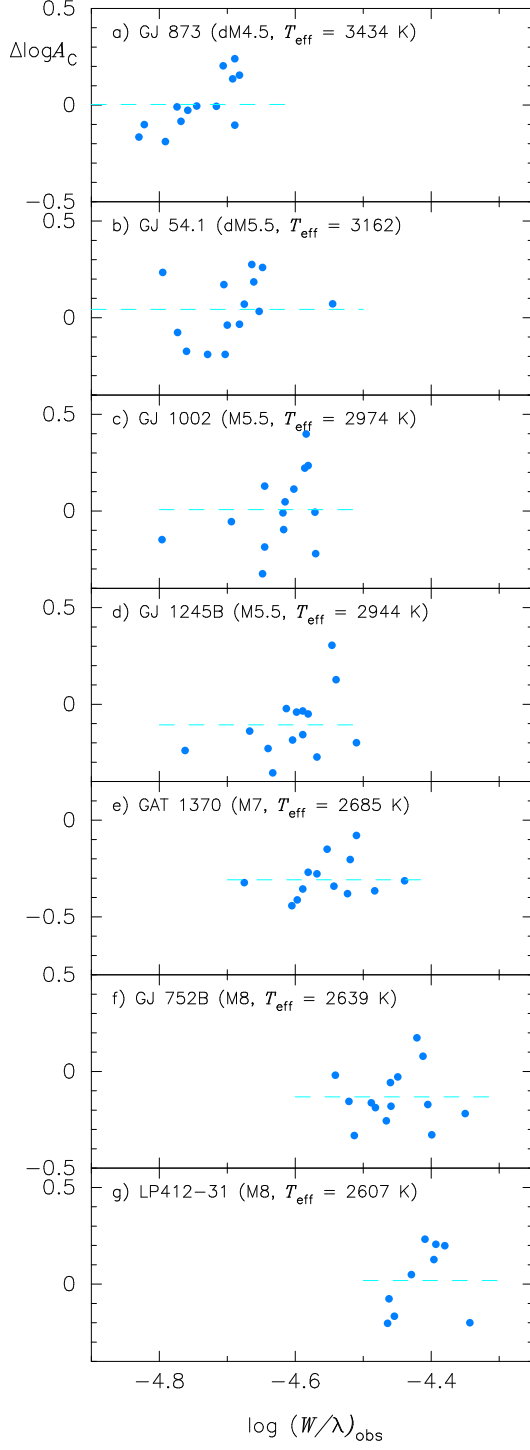


Fig. 7. The resulting logarithmic abundance corrections $\Delta \log A_C$ by the mini curves-of-growth for the CO blends plotted against the observed values of $\log (W/\lambda)_{\text{obs}}$. A dashed line shows the mean correction. a) GJ 873, b) GJ 54.1, c) GJ 1002, d) GJ 1245B, e) GAT 1370, f) GJ 752B, and g) LP 412-31.

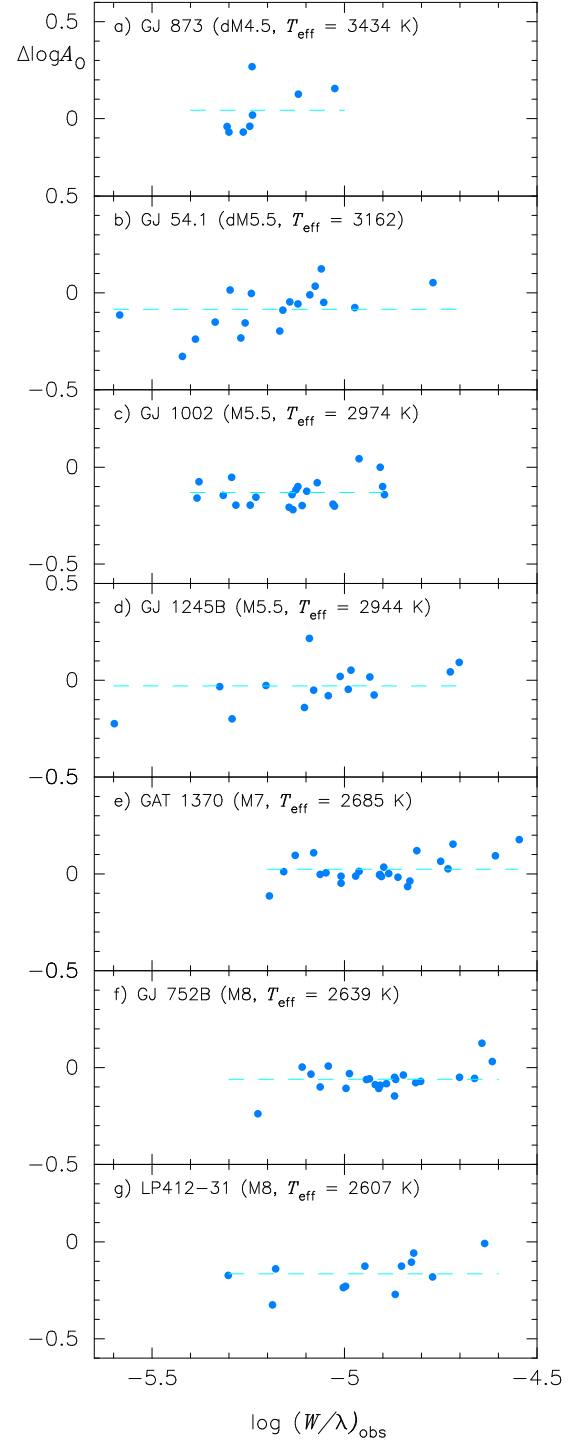


Fig. 8. The resulting logarithmic abundance corrections $\Delta \log A_O$ by the mini curves-of-growth for the H₂O blends in region B plotted against the observed values of $\log (W/\lambda)_{\text{obs}}$. A dashed line shows the mean correction. a) GJ 873, b) GJ 54.1, c) GJ 1002, d) GJ 1245B, e) GAT 1370, f) GJ 752B, and g) LP 412-31.

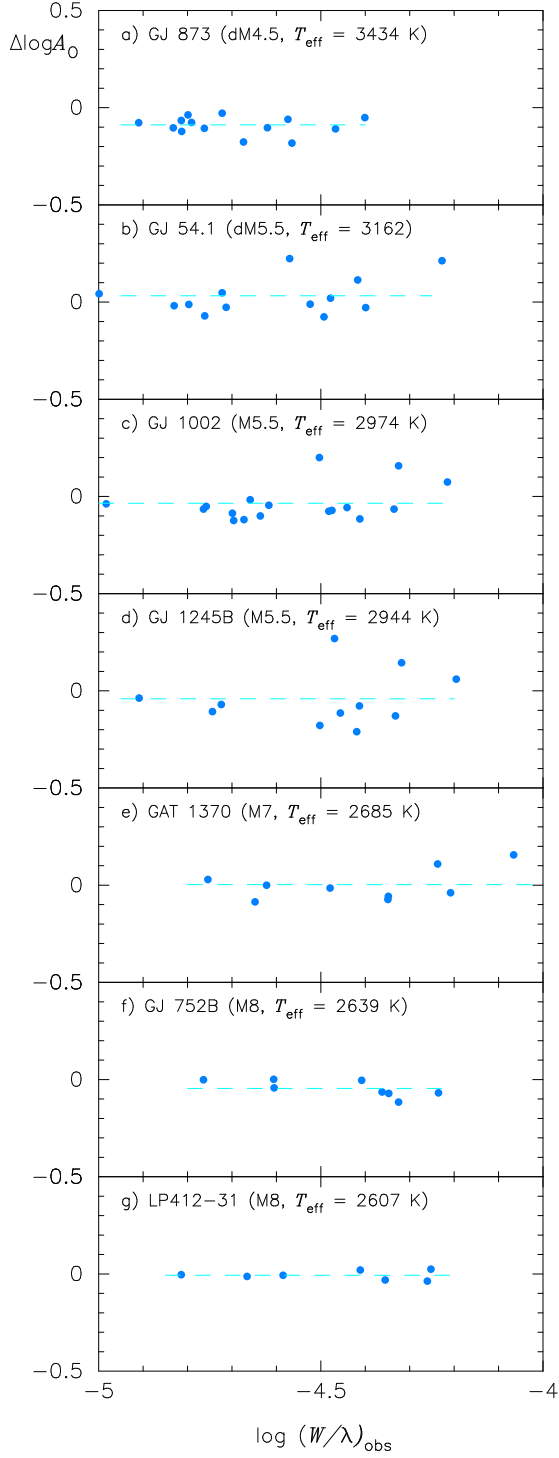


Fig. 9. The resulting logarithmic abundance corrections $\Delta \log A_O$ by the mini curves-of-growth for the H_2O blends in region A plotted against the observed values of $\log (W/\lambda)_{\text{obs}}$. A dashed line shows the mean correction. a) GJ 873, b) GJ 54.1, c) GJ 1002, d) GJ 1245B, e) GAT 1370, f) GJ 752B, and g) LP 412-31.

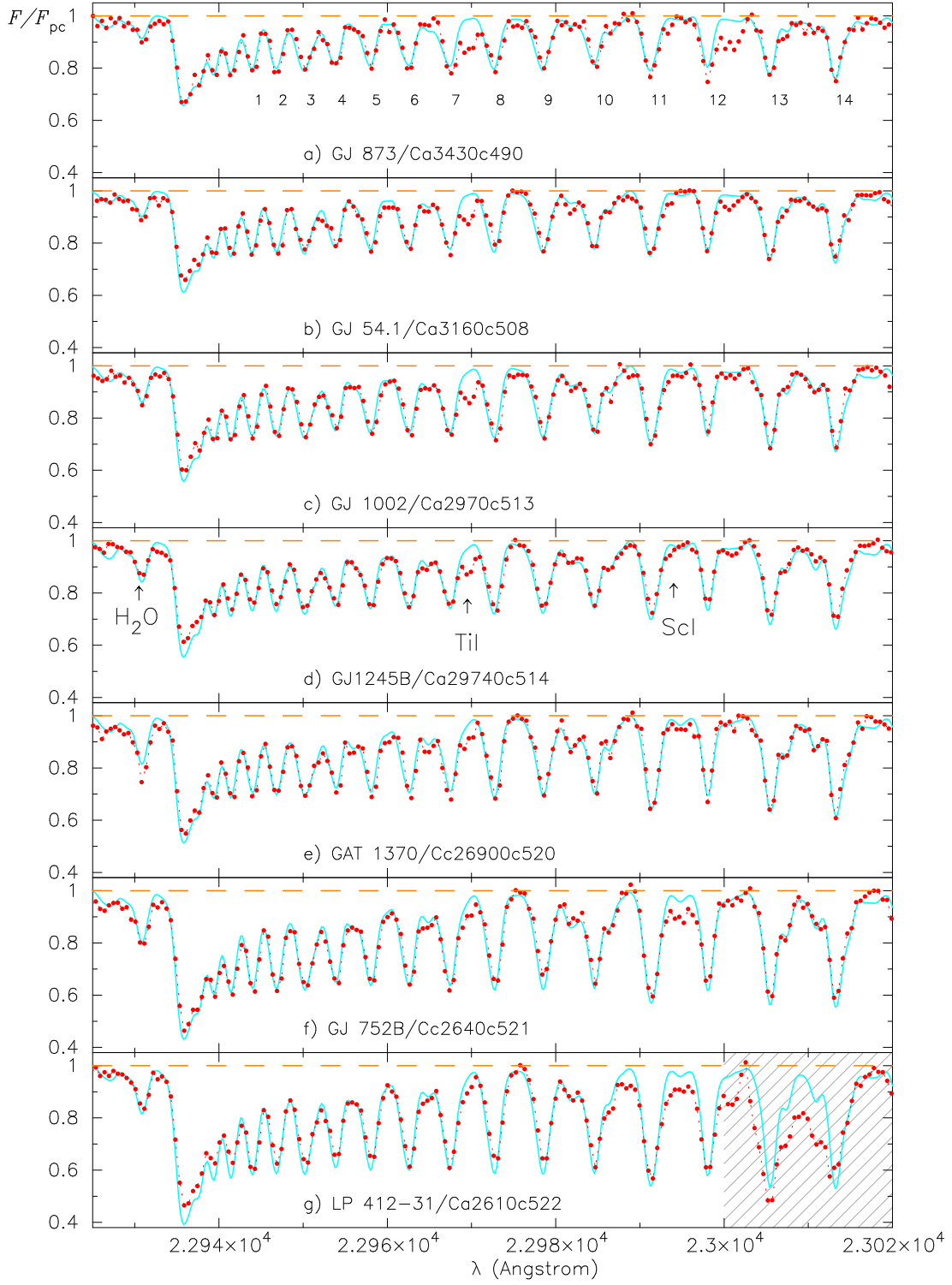


Fig. 10. Comparisons of the observed (filled circles) and predicted (solid line) CO spectra for the final carbon (table 6) and oxygen (table 8) abundances by the mini-CG method are shown for seven late M dwarfs: a) GJ 873, b) GJ 54.1, c) GJ 1002, d) GJ 1245B, e) GAT 1370, f) GJ 752B, and g) LP 412-31 (hatched region remains unexplained).

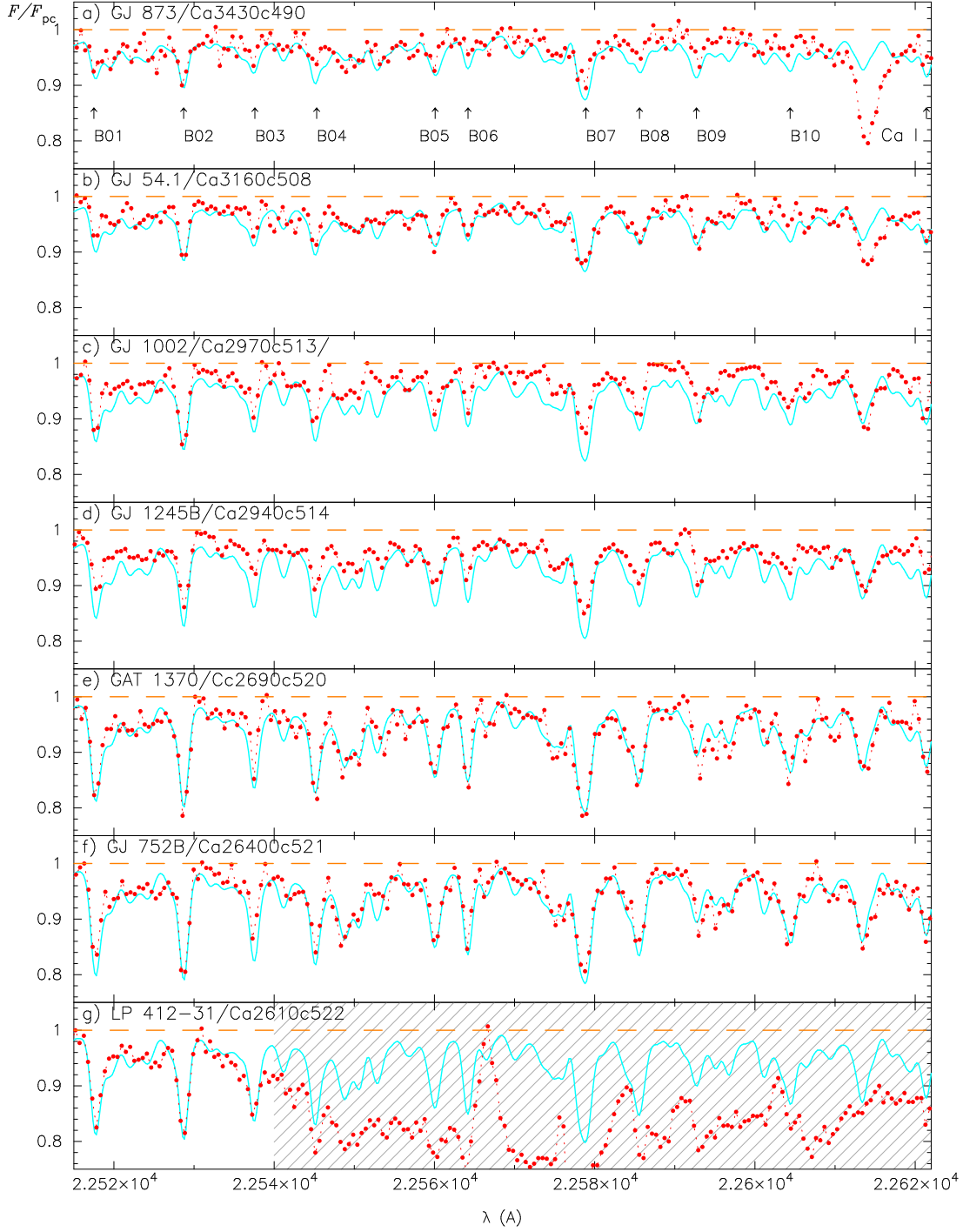


Fig. 11. Comparisons of the observed (filled circles) and predicted (solid line) H₂O spectra in region B for the final carbon (table 6) and oxygen (table 8) abundances by the mini-CG method are shown for seven late M dwarfs: a) GJ 873, b) GJ 54.1, c) GJ 1002, d) GJ 1245B, e) GAT 1370, f) GJ 752B, and g) LP 412-31 (hatched region is disturbed by unknown origin).

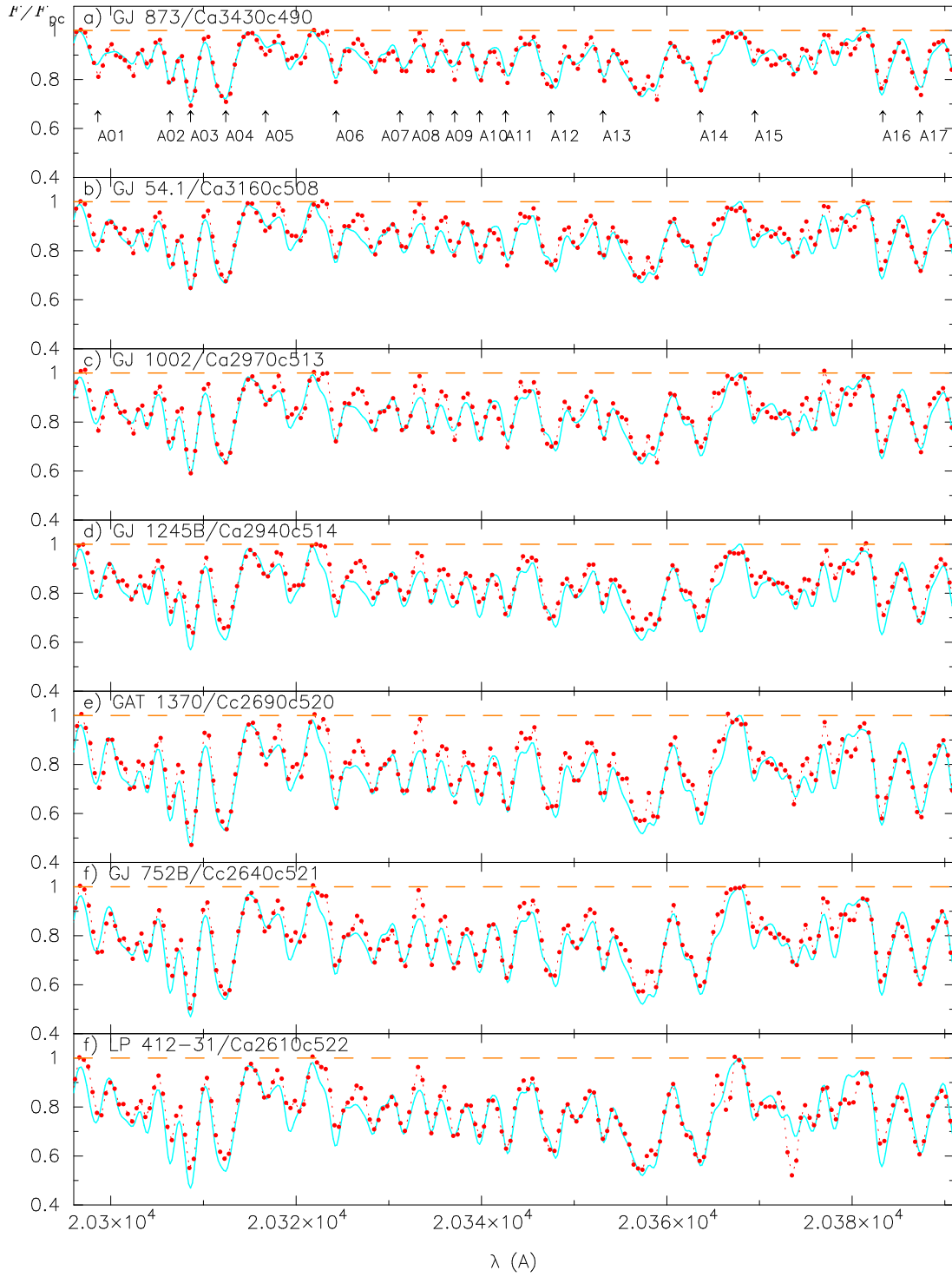


Fig. 12. Comparisons of the observed (filled circles) and predicted (solid line) H_2O spectra in region A for the final carbon (table 6) and oxygen (table 10) abundances by the mini-CG method are shown for seven late M dwarfs: a) GJ 873, b) GJ 54.1, c) GJ 1002, d) GJ 1245B, e) GAT 1370, f) GJ 752B, and g) LP 412-31.

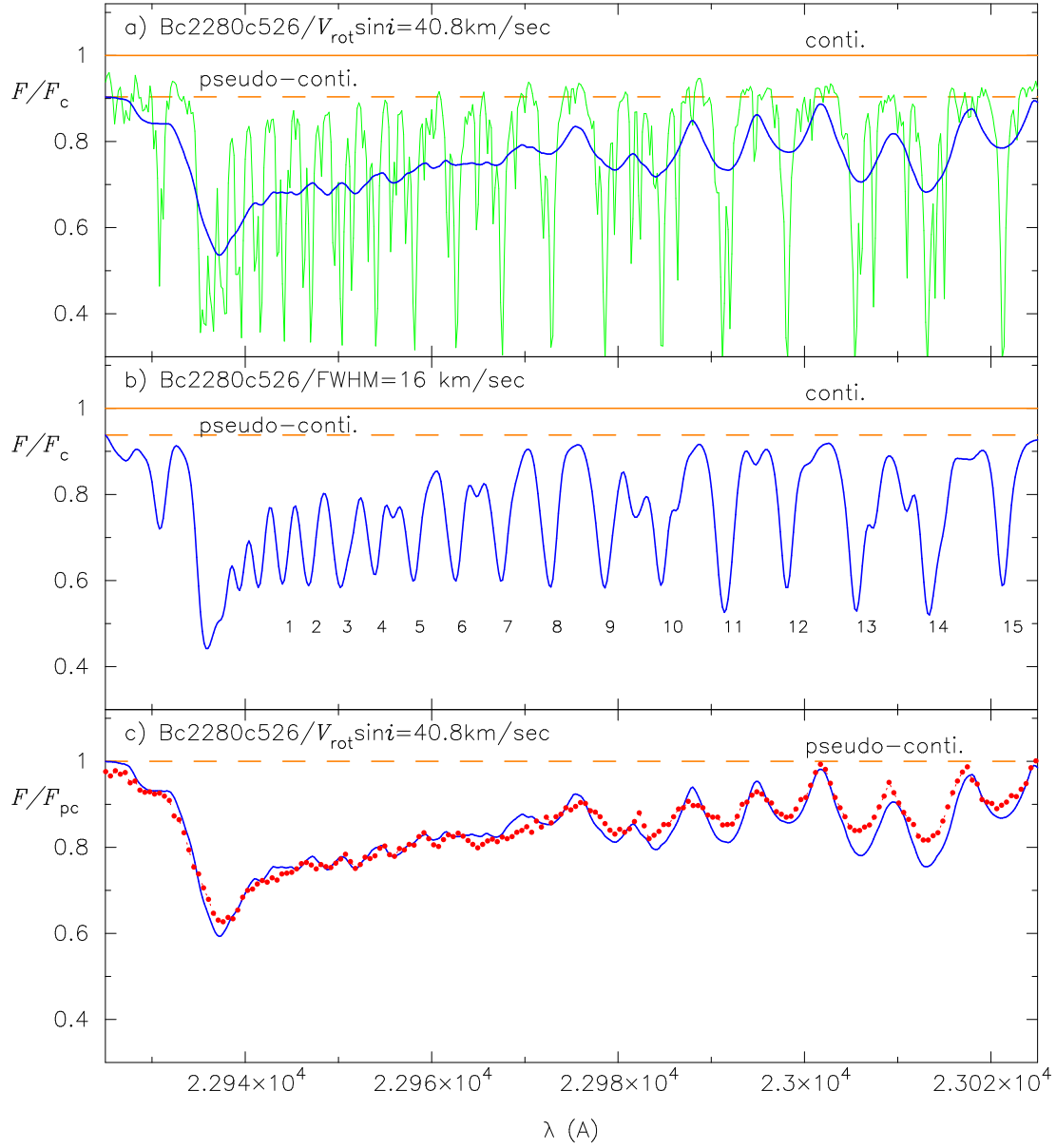


Fig. 13. a) The theoretical spectrum of CO (including the weak H₂O lines) based on the dusty model Bc2280c526 evaluated with a sampling interval of 0.02 \AA (thin line) is convolved with the rotation profile of $V_{\text{rot}} \sin i = 40.8 \text{ km s}^{-1}$ (thick line). b) For comparison, the same theoretical spectrum above is convolved with the slit function (Gaussian) of $\text{FWHM} = 16 \text{ km s}^{-1}$. The numbers attached are the ref. numbers for CO blends (table 7 of Paper I and table 14 in Appendix 1). c) The observed spectrum of 2MASS 1835+32 (dots) is compared with the theoretical spectrum broadened by rotation (thick line from a) above). Note that the theoretical spectrum is based on the solar abundances of $\log A_{\text{C}} = -3.61$ and $\log A_{\text{O}} = -3.31$.

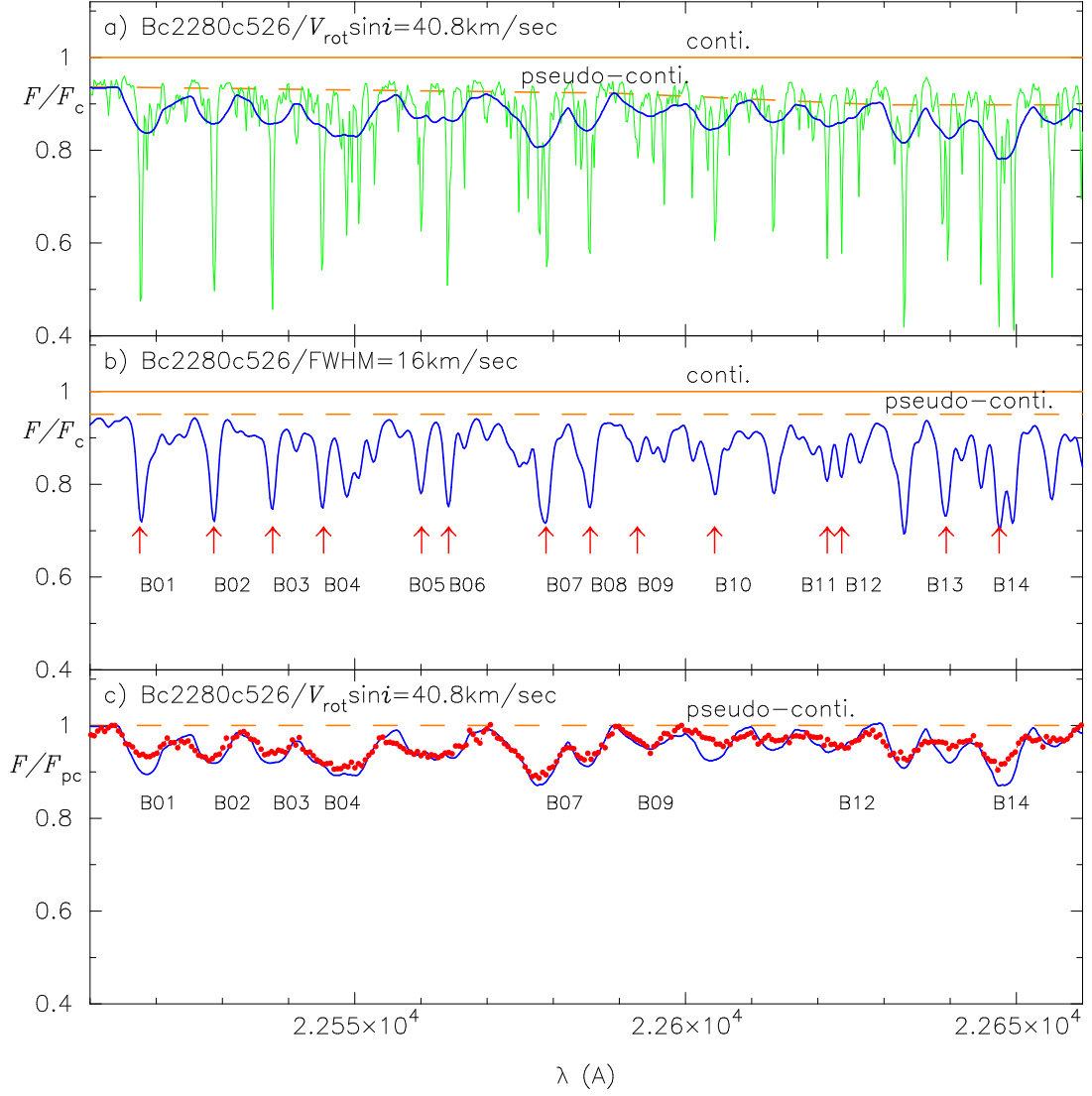


Fig. 14. a) The theoretical spectrum of H_2O based on the dusty model Bc2280c526 evaluated with a sampling interval of 0.02 \AA (thin line) is convolved with the rotation profile of $V_{\text{rot}} \sin i = 40.8 \text{ km s}^{-1}$ (thick line). b) For comparison, the same theoretical spectrum is convolved with the slit function (Gaussian) of $\text{FWHM} = 16 \text{ km s}^{-1}$. The numbers attached are the ref. numbers for H_2O blends (table 4 of Paper II). c) The observed spectrum of 2MASS 1835+32 (dots) is compared with the theoretical spectrum broadened by rotation (thick line from a) above). Note that the theoretical spectrum is based on the solar abundances of $\log A_{\text{C}} = -3.61$ and $\log A_{\text{O}} = -3.31$.

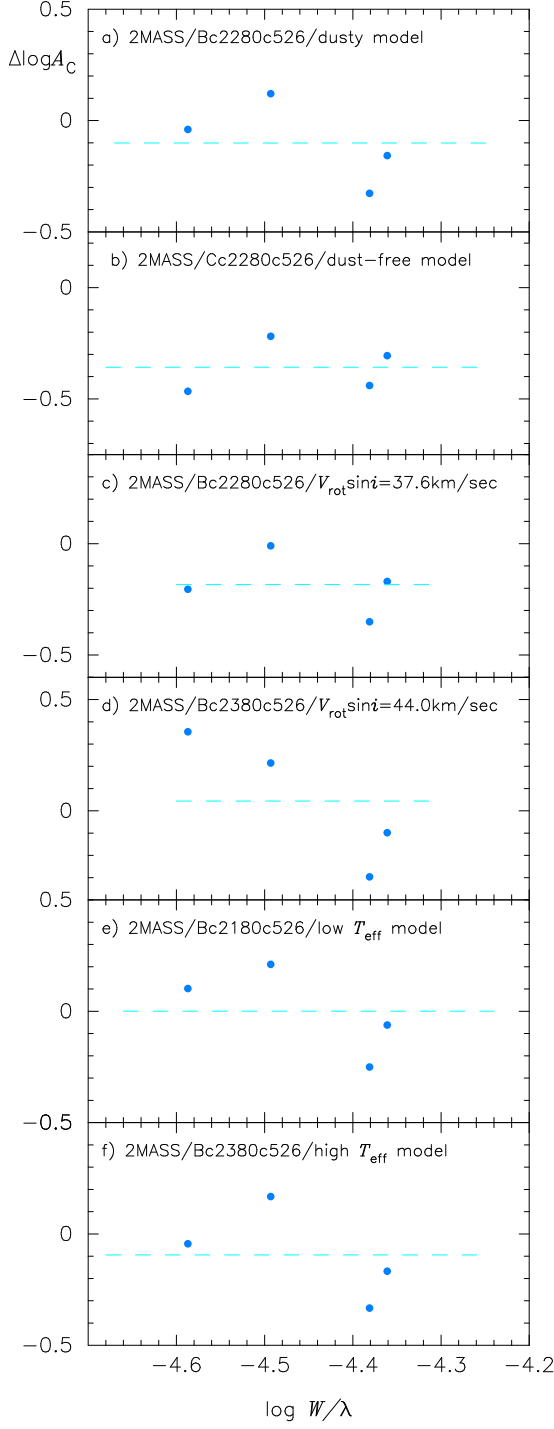


Fig. 15. The resulting logarithmic abundance corrections $\Delta \log A_C$ by the mini curves-of-growth for the CO blends in 2MASS 1835+32 plotted against the observed values of $\log (W/\lambda)_{\text{obs}}$. A dashed line shows the mean correction. a) Based on the dusty model Bc2280c526 and $V_{\text{rot}} \sin i = 40.8 \text{ km s}^{-1}$. b) Based on the dust-free model Cc2280c526 and $V_{\text{rot}} \sin i = 40.8 \text{ km s}^{-1}$. c) Based on the dusty model Bc2280c526 and $V_{\text{rot}} \sin i = 37.6 \text{ km s}^{-1}$ (i.e., lower $V_{\text{rot}} \sin i$). d) Based on the dusty model Bc2280c526 and $V_{\text{rot}} \sin i = 44.0 \text{ km s}^{-1}$ (i.e., higher $V_{\text{rot}} \sin i$). e) Based on the dusty model Bc2180c528 (i.e., lower T_{eff}) and $V_{\text{rot}} \sin i = 40.8 \text{ km s}^{-1}$. f) Based on the dusty model Bc2380c525 (i.e., higher T_{eff}) and $V_{\text{rot}} \sin i = 40.8 \text{ km s}^{-1}$.

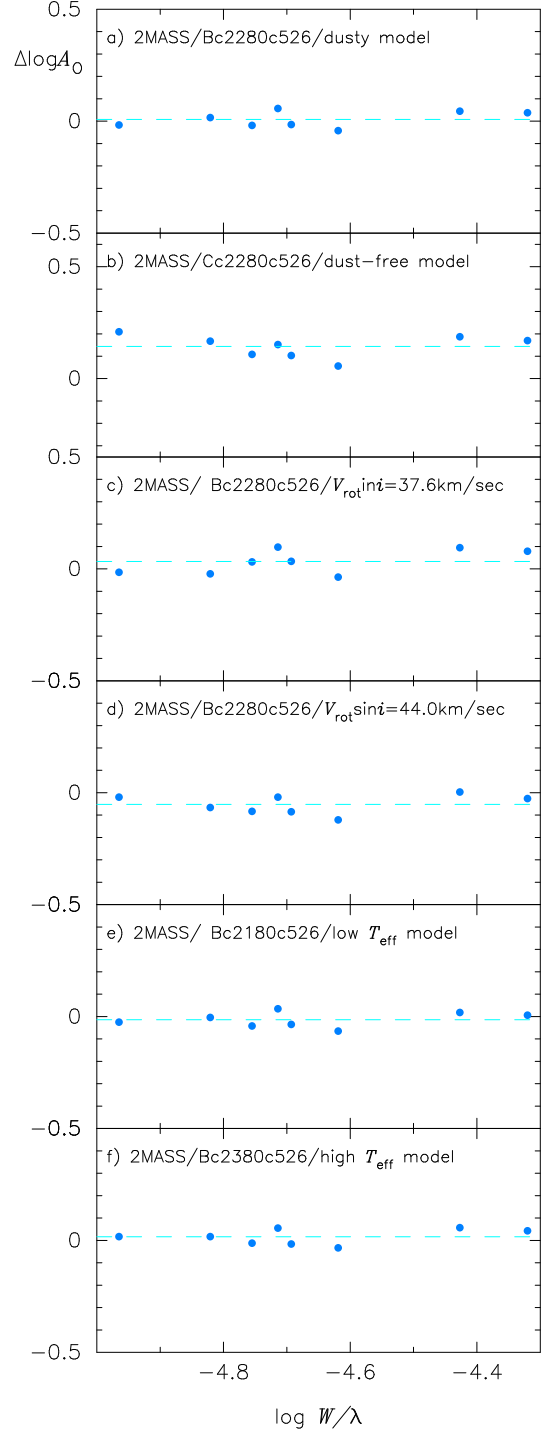


Fig. 16. The resulting logarithmic abundance corrections $\Delta \log A_O$ by the mini curves-of-growth of the H_2O blends in 2MASS 1835+32 plotted against the observed values of $\log (W/\lambda)_{\text{obs}}$. A dashed line shows the mean correction. a) Based on the dusty model Bc2280c526 and $V_{\text{rot}} \sin i = 40.8 \text{ km s}^{-1}$. b) Based on the dust-free model Cc2280c526 and $V_{\text{rot}} \sin i = 40.8 \text{ km s}^{-1}$. c) Based on the dusty model Bc2280c526 and $V_{\text{rot}} \sin i = 37.6 \text{ km s}^{-1}$. d) Based on the dusty model Bc2280c526 and $V_{\text{rot}} \sin i = 44.0 \text{ km s}^{-1}$. e) Based on the dusty model Bc2180c528 and $V_{\text{rot}} \sin i = 40.8 \text{ km s}^{-1}$. f) Based on the dusty model Bc2380c525 and $V_{\text{rot}} \sin i = 40.8 \text{ km s}^{-1}$.

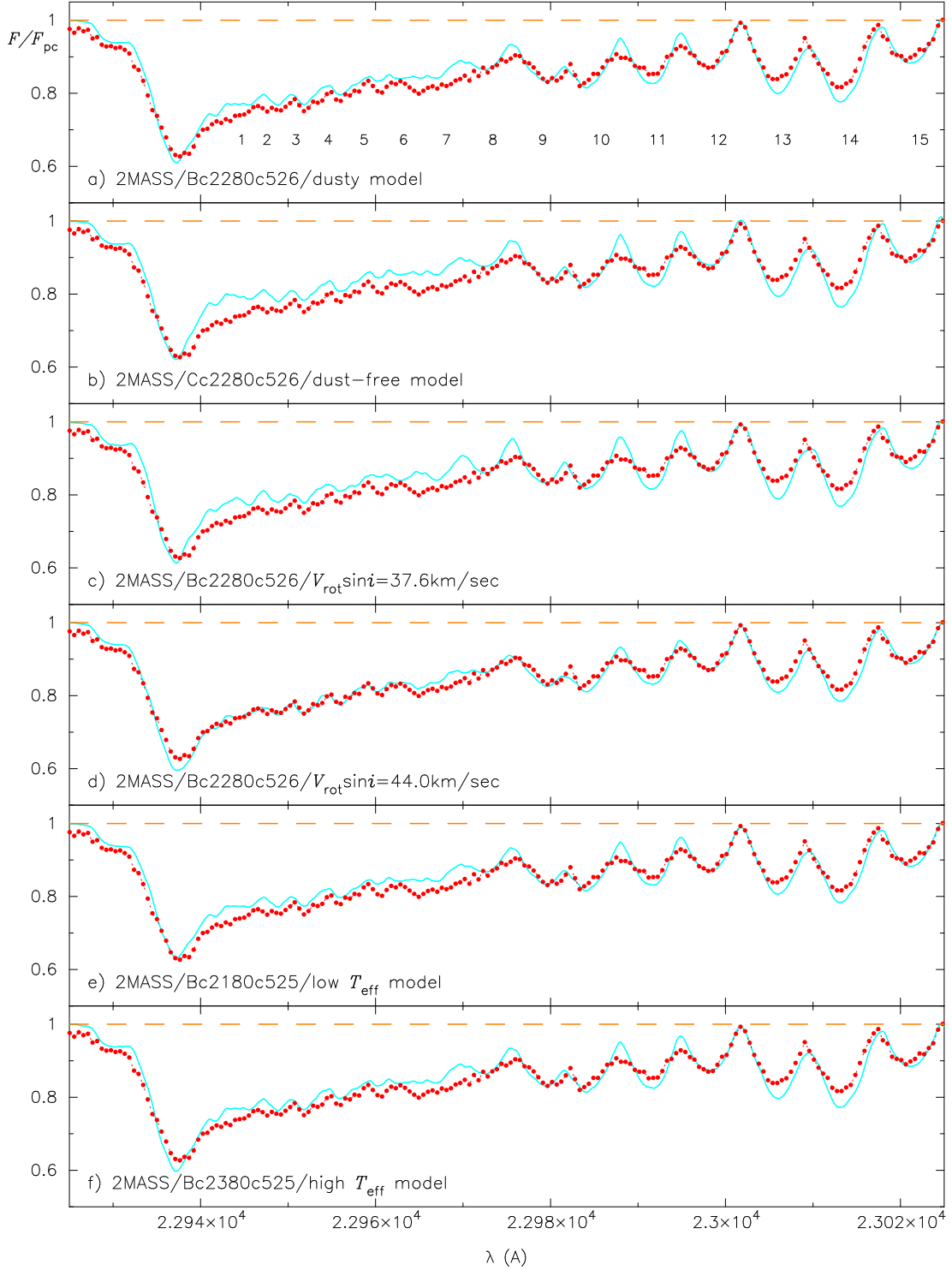


Fig. 17. Comparison of the observed (dots) and predicted (solid line) spectra of CO in 2MASS 1835+32 based on: a) The dusty model Bc2280c526 with $\log A_C$ and $\log A_O$ in table 12 (line no. 1) and $V_{\text{rot}} \sin i = 40.8 \text{ km s}^{-1}$. b) The dust-free model Cc2280c526 with $\log A_C$ and $\log A_O$ in table 12 (line no. 2) and $V_{\text{rot}} \sin i = 40.8 \text{ km s}^{-1}$. c) The dusty model Bc2280c526 with $\log A_C$ and $\log A_O$ in table 12 (line no. 3) and $V_{\text{rot}} \sin i = 37.6 \text{ km s}^{-1}$. d) The dusty model Bc2280c526 with $\log A_C$ and $\log A_O$ in table 12 (line no. 4) and $V_{\text{rot}} \sin i = 44.0 \text{ km s}^{-1}$. e) The dusty model Bc2180c528 with $\log A_C$ and $\log A_O$ in table 12 (line no. 5) and $V_{\text{rot}} \sin i = 40.8 \text{ km s}^{-1}$. f) The dusty model Bc2380c525 with $\log A_C$ and $\log A_O$ in table 12 (line no. 6) and $V_{\text{rot}} \sin i = 40.8 \text{ km s}^{-1}$.

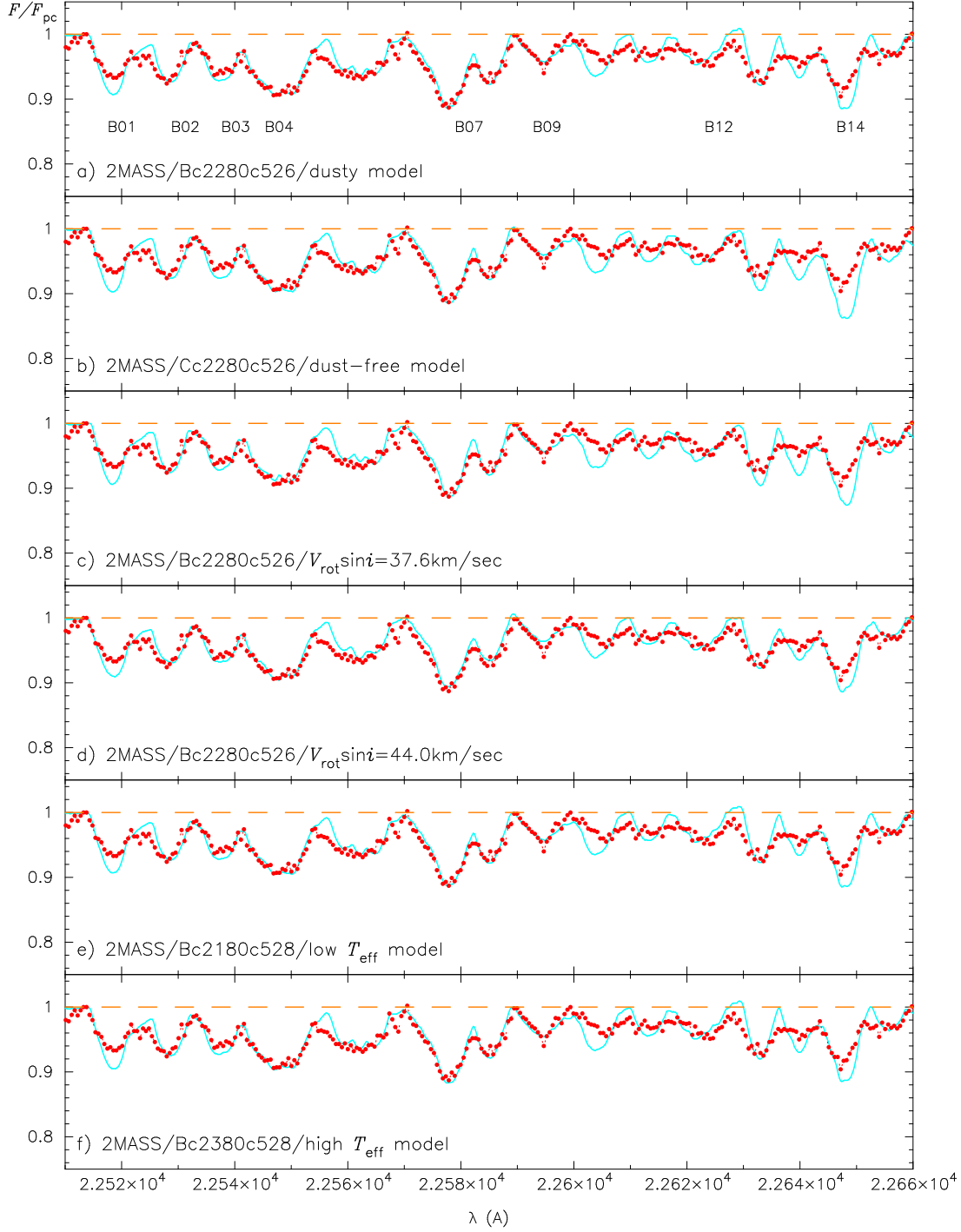


Fig. 18. Comparison of the observed (dots) and predicted (solid line) spectra of H₂O in 2MASS 1835+32 based on: a) The dusty model Bc2280c526 with $\log A_C$ and $\log A_O$ in table 12 (line no. 1) and $V_{\text{rot}} \sin i = 40.8 \text{ km s}^{-1}$. b) The dust-free model Cc2280c526 with $\log A_C$ and $\log A_O$ in table 12 (line no. 2) and $V_{\text{rot}} \sin i = 40.8 \text{ km s}^{-1}$. c) The dusty model Bc2280c526 with $\log A_C$ and $\log A_O$ in table 12 (line no. 3) and $V_{\text{rot}} \sin i = 37.6 \text{ km s}^{-1}$. d) The dusty model Bc2280c526 with $\log A_C$ and $\log A_O$ in table 12 (line no. 4) and $V_{\text{rot}} \sin i = 44.0 \text{ km s}^{-1}$. e) The dusty model Bc2180c528 with $\log A_C$ and $\log A_O$ in table 12 (line no. 5) and $V_{\text{rot}} \sin i = 40.8 \text{ km s}^{-1}$. f) The dusty model Bc2380c525 with $\log A_C$ and $\log A_O$ in table 12 (line no. 6) and $V_{\text{rot}} \sin i = 40.8 \text{ km s}^{-1}$.

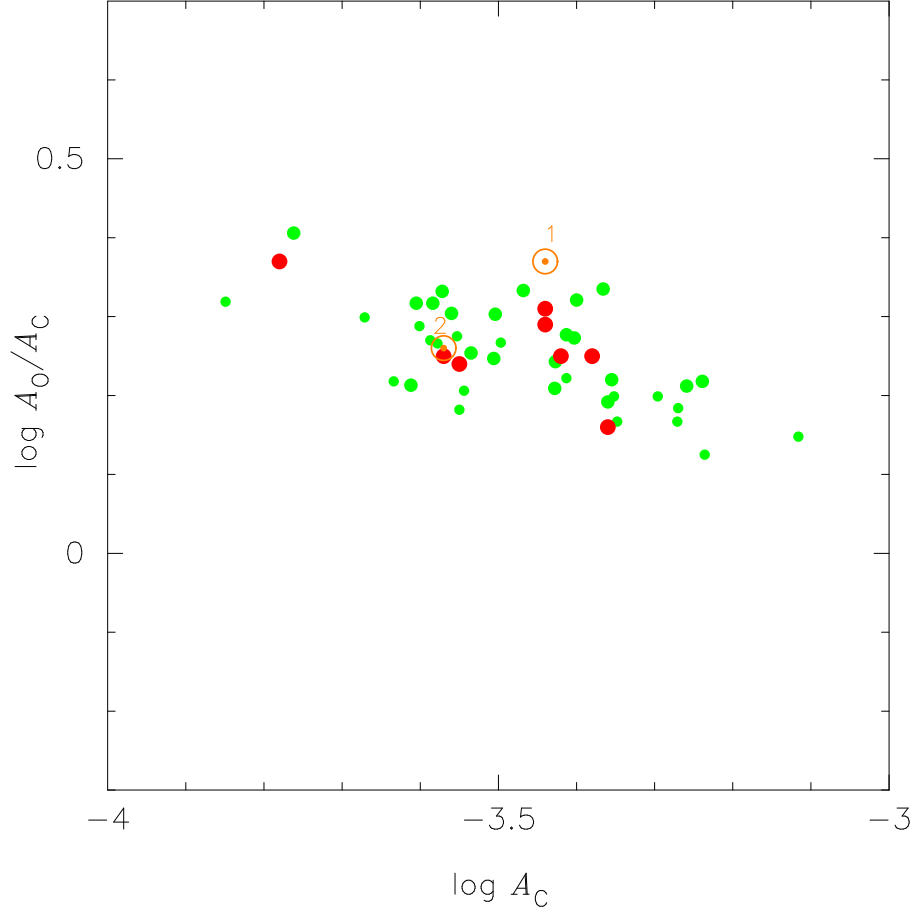


Fig. 19. The oxygen-to-carbon ratios in eight late M dwarfs from table 19 are plotted against the carbon abundances $\log A_C$ by red (or black) filled circles. Those in the early and middle M dwarfs from Paper II are shown by green (or grey) filled circles. The solar values based on the classical (Anders & Grevesse 1989) and more recent result (Asplund et al. 2009) are also shown by \odot mark with 1 and 2, respectively.

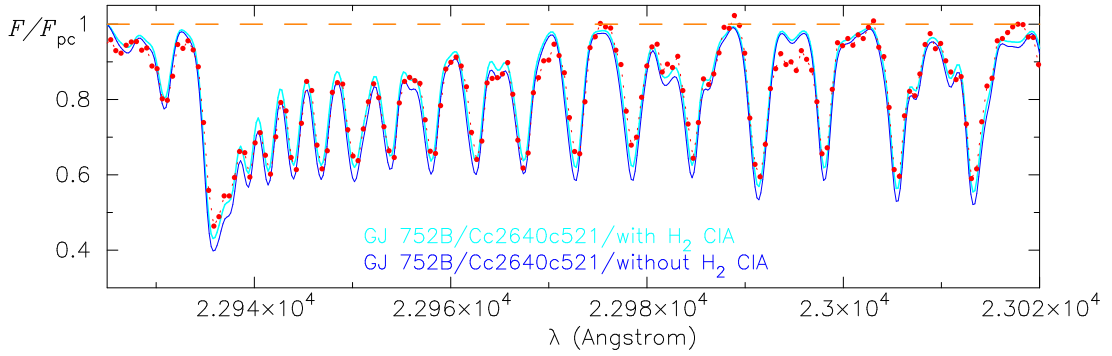


Fig. 20. The predicted spectrum of CO based on the photospheric model Cc2640c521 and $\log A_C = -3.550$ (table 6) but disregarding the H_2 CIA (blue/black solid line) is compared with the one based on the same model and $\log A_C$ but including the H_2 CIA (light sky/grey solid line). The observed spectrum of GJ 752B is shown by filled circles.

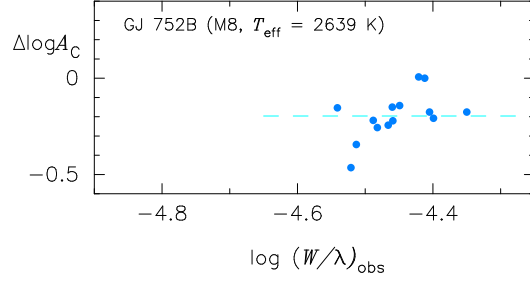


Fig. 21. The logarithmic abundance corrections $\Delta \log A_C$ to the value of $\log A_C = -3.550$ (based on the normal analysis of GJ 752B including the H_2 CIA) needed to explain the observed EWs of CO blends by the use of the model photosphere Cc2640c521 disregarding the H_2 CIA. The resulting $\Delta \log A_C = -0.196 \pm 0.081$ implies that the neglect of H_2 CIA results in an error of -0.20 dex in $\log A_C$.

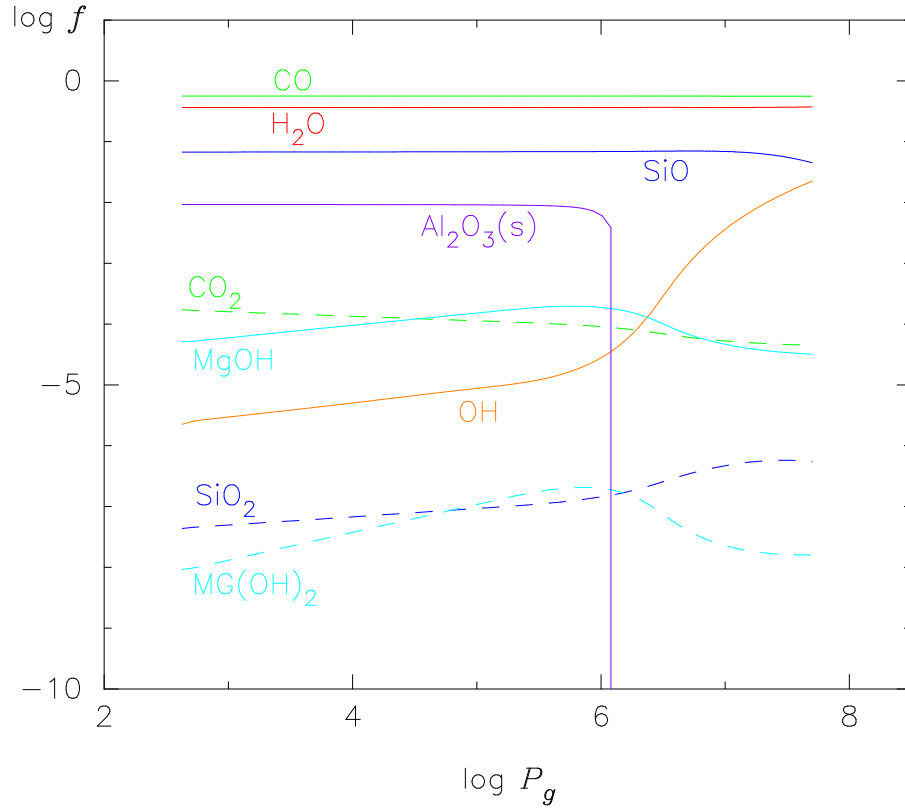


Fig. 22. Logarithm of the fraction f (defined by equation 7 in the text) of oxygen atoms in the major molecules and grains consuming oxygen plotted against $\log P_g$ in the model photosphere Bc2280c526 of the M8.5 dwarf 2 MASS 1835+32. Most oxygen atoms are depleted into CO, H_2O , and SiO molecules, and about 1% of oxygen atoms are in corundum (Al_2O_3). Enstatite (MgSiO_3) does not form in this model yet (see figure 5).

Table 1. Target stars.

Name	Other Name	K mag	SNR(28th)	SNR(25th)	LGS*
GJ 54.1	YZ Cet	6.42	63	53	
GJ 752B	vB10	8.77	105	156	
GJ 873	EV Lac	5.30	94	40	
GJ 1002	LHS 2	7.44	139	142	
GJ 1245B	LHS 3495	7.39	63	50	
GAT 1370	Teegarden's star	7.59	84	88	
LP 412-31		10.64	31	66	Y
2MASS 1835+32 [†]		9.17	87	67	Y

* A laser guide star was used, if Y.

[†] Abbreviation of 2MASS J18353790+3259545.**Table 2.** Eechlle setting.

Order	Wavelength range (Å)	Dispersion (Å pixel ⁻¹)
29th	19397–19867	0.460
28th	20089–20575	0.475
27th	20833–21335	0.491
26th	21634–22154	0.508
25th	22500–23039	0.527
24th	23437–23997	0.547
23rd	24456–25038	0.569

Table 3. Fundamental parameters of the program stars.

obj.	sp.type*	p (msec) [†]	$F_{3.4}$ (mag) [‡]	$M_{3.4}$ (mag) [§]	T_{eff}	R/R_{\odot} [#]	M/M_{\odot} ^{**}	$\log g$
GJ 54.1	dM5.5e	271.010 ± 8.360	6.167 ± 0.044	8.33 ± 0.11	3162.	0.177	0.139	5.084
GJ 752B	M8	170.360 ± 1.000	8.317 ± 0.020	9.47 ± 0.03	2639.	0.123	0.090	5.213
GJ 873	dM4.5e	195.220 ± 1.870	5.241 ± 0.063	6.69 ± 0.08	3434.	0.353	0.363	4.903
GJ 1002	M5.5	213.000 ± 3.600	7.176 ± 0.028	8.82 ± 0.06	2974.	0.153	0.116	5.133
GJ 1245B	M5.5	220.000 ± 1.000	7.178 ± 0.066	8.89 ± 0.08	2944.	0.151	0.114	5.138
GAT 1370	M8/9	260.630 ± 2.690	7.322 ± 0.027	9.40 ± 0.05	2685.	0.128	0.094	5.199
LP 412-31	M8	68.300 ± 0.600	10.352 ± 0.023	9.52 ± 0.04	2607.	0.122	0.089	5.217
2MASS 1835+32	M8.5	176.5 ± 0.5	8.837 ± 0.020	10.07 ± 0.03	2275.	0.112	0.083	5.261

* dM by Joy & Abt (1974), and M by SIMBAD.

[†] By Hipparcos (van Leeuwen 2007), except for 2MASS 1835+32 by RECONS.[‡] $W1$ band flux centered at 3.4 μm from the WISE All-Sky Release for $F_{3.4} < 8.0$ mag and from the AllWISE catalog for $F_{3.4} > 8.0$ mag (Wright et al. 2010).[§] Absolute magnitude at 3.4 μm based on $F_{3.4}$.^{||} Based on $M_{3.4} - \log T_{\text{eff}}$ relation shown by the dashed line in figure 1 of Paper I for $M_{3.4} < 9.0$ and based on the solid line in figure 1a for $M_{3.4} > 9.0$.[#] Based on radius – $\log T_{\text{eff}}$ relation of equation 8 by Boyajian et al. (2012) for dM4.5 – dM6, and on the solid line in figure 3 for dM7 – dM8.5.^{**} Based on mass – radius relation of equation 10 by Boyajian et al. (2012) and on the solid line in figure 4.

Table 4. Fundamental parameters of the calibration objects.

no.	obj.	other name	$p(\text{msec})^*$	$F_{3.4}(\text{mag})^\dagger$	$M_{3.4}(\text{mag})^\ddagger$	T_{eff}^\S	$\log f_{\text{bol}}^\parallel$	$\log L/L_\odot^\#$	R/R_\odot^{**}	$K^{\dagger\dagger}$	$M_K^{\ddagger\dagger}$	$M/M_\odot^{\S\S}$
1	GJ 406	Wolf 359	419.1	5.807	8.92	2800.	-8.221	-2.975	0.139	6.08	9.19	0.103
2	GJ 644C	vB 8	148.92	8.619	9.48	2640.	-9.329	-3.184	0.123	8.82	9.69	0.090
3	GJ 752B	vB 10	170.36	8.317	9.47	2250.	-9.422	-3.394	0.133	8.80	9.96	0.088
4	GJ 3849	LHS 2924	95.0	10.428	10.32	2130.	-10.210	-3.675	0.107	10.67	10.56	0.080

* Parallax by RECONS for GJ 406 and GJ 644C, by Hipparcos (van Leeuwen 2007) for GJ 752B, and by Gliese & Jahreiss (1991) for GJ 3849.

† W1 band flux centered at $3.4\mu\text{m}$ from the WISE All-Sky Release for $F_{3.4} < 8.0$ mag and from the AllWISE catalog for $F_{3.4} > 8.0$ mag (Wright et al. 2010).

‡ Absolute magnitude at $3.4\mu\text{m}$ based on $F_{3.4}$.

§ Based on the infrared flux method (Tsuiji et al. 1996a).

$^\parallel$ Observed bolometric flux based on the integration of SED (Tsuiji et al. 1996a).

$^\#$ Bolometric luminosity based on the third and seventh columns.

** Based on L/L_\odot and T_{eff} .

†† Observed K magnitude (Leggett 1992).

‡† Absolute magnitude at K .

§§ Based on $M_K - M/M_\odot$ of Delfosse et al. (2000) extended by the use of $M_K - M/M_\odot$ from the evolutionary models of Baraffe et al. (1998). see figure 2.

Table 5. $\log(W/\lambda)_{\text{obs}}^*$ of CO blends (2-0 band) in 8 late M dwarfs.

Ref. no †	GJ 54.1	GJ 752B	GJ 873	GJ 1002	GJ 1245B	GAT 1370	LP 412-31	2MASS 1835+32
1	-4.705	-4.460	-4.774	-4.645	-4.613	-4.581	-4.393	—
2	-4.661	-4.459	-4.758	-4.615	-4.581	-4.519	-4.454	—
3	-4.545	-4.350	-4.689	-4.570	-4.510	-4.439	-4.343	—
4	-4.664	-4.421	-4.706	-4.584	-4.546	-4.553	-4.409	—
5	-4.648	-4.449	-4.830	-4.602	-4.540	-4.589	-4.429	—
6	-4.700	-4.482	-4.768	-4.618	-4.640	-4.597	-4.396	—
7	-4.675	-4.412	-4.692	-4.581	-4.598	-4.510	-4.380	—
8	-4.760	-4.488	-4.689	-4.586	-4.589	-4.568	-4.462	—
9	-4.729	-4.513	-4.791	-4.645	-4.604	-4.605	-4.464	—
10	-4.773	-4.521	-4.822	-4.694	-4.667	—	—	—
11	-4.653	-4.405	-4.682	-4.571	-4.633	-4.523	—	—
12	-4.795	-4.541	—	-4.796	-4.762	-4.675	—	-4.493
13	-4.682	-4.466	-4.745	-4.617	-4.589	-4.543	—	-4.361
14	-4.703	-4.399	-4.716	-4.648	-4.568	-4.483	—	-4.381
15	—	—	—	—	—	—	—	-4.587

* The equivalent width W is measured by referring to the pseudo-continuum.

† Ref. nos. defined in table 7 and figure 4 of Paper I, except for ref. no.15 defined in table 14 (Appendix 1) and figure 13b.

Table 6. Carbon abundances from the CO lines.

obj.	T_{eff}	$\log g$	model1*	$\Delta \log A_C^{(1)\dagger}$	$\log A_C^{(1)}$	model2 ‡	$\Delta \log A_C^{(2)\S}$	$\log A_C^{(2)}$	N^\parallel	$\chi^2\#$
GJ 54.1	3162.	5.084	Ca3200c50	+0.042	-3.358 \pm 0.112	Ca3160c508	-0.022	-3.380 \pm 0.086	14	1.511
GJ 752B	2639.	5.213	Ca2600c525	-0.131	-3.531 \pm 0.098	Cc2640c521	-0.019	-3.550 \pm 0.066	14	20.114
GJ 873	3434.	4.903	Ca3400c50	-0.003	-3.397 \pm 0.094	Ca3430c490	-0.043	-3.440 \pm 0.092	13	1.474
GJ 1002	2974.	5.133	Ca3000c50	+0.007	-3.393 \pm 0.135	Ca2970c513	-0.024	-3.417 \pm 0.088	14	14.710
GJ 1245B	2944.	5.138	Ca2900c525	-0.107	-3.507 \pm 0.116	Ca2940c514	+0.072	-3.435 \pm 0.098	14	1.372
GAT 1370	2685.	5.199	Ca2700c525	-0.301	-3.701 \pm 0.071	Cc2690c520	-0.080	-3.781 \pm 0.061	13	5.716
LP 412-31	2607.	5.217	Ca2600c525	+0.019	-3.381 \pm 0.123	Ca2610c522	+0.022	-3.357 \pm 0.068	9	17.296

* Model photosphere from the UCM grid.

† First correction to the assumed values for the model of the Ca series; $\log A_C^{(0)} = -3.40$ and $\log A_O^{(0)} = -3.08$.

‡ Specified model for T_{eff} and $\log g$ in the second and third columns, respectively.

§ Second correction to the starting values $\log A_C = \log A_C^{(1)}$ in the sixth column of table 6 and $\log A_O = \log A_O^{(1)}$ in the fourth column of table 8.

$^\parallel$ Number of CO blends used for the mini-CG analysis.

$^\#$ χ^2 value for the comparison of the observed and predicted spectra in figure 10.

Table 7. $\log(W/\lambda)_{\text{obs}}^*$ of H₂O blends in region B for 8 late M dwarfs.

Ref. no [†]	GJ 54.1	GJ 752B	GJ 873	GJ 1002	GJ 1245B	GAT 1370	LP 412-31	2MASS 1835+32
B01	—	-4.870	—	-5.026	—	-4.830	-4.868	-4.693
B02	—	-5.225	—	—	—	—	-5.187	-4.714
B03	-5.336	-4.911	—	-5.121	-5.011	-4.885	-4.852	-4.755
B04	-5.142	-4.870	-5.120	-4.962	-4.983	-4.812	-4.820	-4.320
B05	-5.387	—	-5.300	—	—	-5.195	—	—
B06	-5.168	-4.867	—	-5.134	-5.042	-4.908	—	—
B07	-5.121	-4.943	—	-5.126	—	-4.962	—	-4.427
B08	-5.242	-5.063	—	-5.315	-5.204	-5.048	—	—
B09	-4.770	-4.662	—	-4.896	-4.725	-4.608	—	-4.965
B10	—	—	—	-5.030	—	—	—	—
B11	—	—	—	—	—	—	—	—
B12	-5.421	—	—	—	—	-4.904	—	-4.821
B13	—	—	—	—	—	—	—	—
B14	—	-4.987	—	-5.282	-5.292	-5.063	—	-4.619
B15	—	-5.087	—	-5.383	-5.598	-5.158	—	—
B16	-5.269	-4.815	-5.263	-5.110	-5.104	-4.750	-4.636	—
B17	-5.054	-4.802	-5.246	-5.144	-4.990	-4.861	—	—
B18	—	-4.907	—	-5.245	—	-5.009	—	—
B19	-5.584	-5.042	-5.240	-5.378	-5.091	-5.080	-5.179	—
B20	-5.090	-4.920	-5.239	-5.071	-5.080	-4.898	-5.003	—
B21	-5.060	-4.935	—	-5.230	—	-5.009	-4.947	—
B22	—	—	—	—	—	—	—	—
B23	-5.258	-4.996	—	-5.136	—	-4.971	—	—
B24	-5.076	-4.847	—	—	—	—	—	—
B25	—	—	—	—	—	—	—	—
B26	-5.160	-4.891	-5.305	-5.098	—	-4.909	-4.997	—
B27	—	—	—	—	—	-4.836	—	—

* The equivalent width W is measured by referring to the pseudo-continuum.[†] Ref. no. defined in table 4 and figure 3 of Paper II.**Table 8.** Oxygen abundances $\log A_{\text{O}}^B$ from the H₂O blends in region B.

obj.	model2*	$\Delta \log A_{\text{O}}^{(1)\dagger}$	$\log A_{\text{O}}^{(1)}$	$\Delta \log A_{\text{O}}^{(2)\ddagger}$	$\log A_{\text{O}}^{(2)}$	N^{\S}	χ^2_{\parallel}
GJ 54.1	Ca3160c508	-0.085	-3.193 ± 0.079	+0.050	-3.143 ± 0.049	18	1.344
GJ 752B	Cc2640c521	-0.060	-3.291 ± 0.046	-0.010	-3.301 ± 0.042	23	13.946
GJ 873	Ca3430c490	+0.043	-3.054 ± 0.085	-0.015	-3.069 ± 0.103	8	2.154
GJ 1002	Ca2970c513	-0.131	-3.224 ± 0.047	+0.071	-3.153 ± 0.036	21	18.918
GJ 1245B	Ca2940c514	-0.029	-3.236 ± 0.076	+0.104	-3.132 ± 0.050	15	2.479
GAT 1370	Cc2690c520	+0.024	-3.377 ± 0.047	-0.037	-3.414 ± 0.059	24	4.305
LP 412-31	Ca2610c522	-0.165	-3.246 ± 0.061	+0.057	-3.189 ± 0.036	12	38.805

* Specified model for T_{eff} and $\log g$ in the second and third columns of table 6, respectively.[†] First correction to the starting value of $\log A_{\text{C}} = \log A_{\text{C}}^{(1)}$ in table 6 and $\log A_{\text{O}} = \log A_{\text{C}}^{(1)} + 0.30$.[‡] Second correction to the starting values $\log A_{\text{C}} = \log A_{\text{C}}^{(2)}$ in the ninth column of table 6 and $\log A_{\text{O}} = \log A_{\text{O}}^{(1)}$ in fourth column of this table.[§] Number of H₂O blends used for the mini-CG analysis.^{||} χ^2 value for the comparison of the observed and predicted spectra in figure 11.

Table 9. $\log(W/\lambda)_{\text{obs}}$ * of H₂O blends in region A for 7 late M dwarfs.

Ref. no [†]	GJ 54.1	GJ 752B	GJ 873	GJ 1002	GJ 1245B	GAT 1370	LP 412-31
A01	-4.797	-4.606	-4.814	-4.758	-4.724	-4.622	-4.666
A02	—	—	-4.791	-4.696	—	—	—
A03	-4.524	-4.347	-4.620	-4.475	-4.456	-4.349	-4.355
A04	-4.399	-4.235	-4.467	-4.335	-4.332	-4.208	-4.260
A05	-4.999	-4.764	-5.047	-4.983	-4.909	-4.754	-4.814
A06	—	—	-4.832	-4.699	—	—	—
A07	-4.713	—	-4.722	-4.617	—	-4.479	—
A08	-4.830	-4.605	-4.910	-4.764	-4.744	-4.648	-4.585
A09	-4.761	—	-4.813	-4.673	—	—	—
A10	—	—	-4.762	-4.636	—	—	—
A11	-4.570	-4.408	—	-4.503	-4.469	—	-4.411
A12	—	—	—	—	—	—	—
A13	-4.493	-4.325	-4.565	-4.412	-4.419	—	—
A14	-4.722	—	-4.799	-4.659	—	—	—
A15	—	—	—	—	—	—	—
A16	—	—	—	—	—	—	—
A17	—	-4.362	-4.674	-4.482	-4.502	-4.348	—

* The equivalent width W is measured by referring to the pseudo-continuum.

[†] Ref. no. defined in table 2 and figure 2 of Paper II.

Table 10. Oxygen abundances $\log A_{\text{O}}^{\text{A}}$ from the H₂O blends in region A.

obj.	model2*	$\Delta \log A_{\text{O}}^{(3)\dagger}$	$\log A_{\text{O}}^{(3)}$	N_{A}^{\ddagger}	$\chi^2_{\text{§}}$
GJ 54.1	Ca3160c508	+0.032	-3.111 ± 0.065	13	4.485
GJ 752B	Cc2640c521	-0.046	-3.347 ± 0.028	8	20.272
GJ 873	Ca3430c490	-0.088	-3.157 ± 0.032	15	7.313
GJ 1002	Ca2970c513	-0.035	-3.188 ± 0.063	17	25.032
GJ 1245B	Ca2940c514	-0.041	-3.173 ± 0.097	11	6.822
GAT 1370	Cc2690c520	+0.003	-3.411 ± 0.056	9	14.985
LP 412-31	Ca2610c522	-0.007	-3.207 ± 0.016	7	1.970

* Specified model for T_{eff} and $\log g$ in the second and third columns of table 6, respectively.

[†] Correction to the starting values $\log A_{\text{C}} = \log A_{\text{C}}^{(2)}$ in the ninth column of table 6 and $\log A_{\text{O}} = \log A_{\text{O}}^{(2)}$ in sixth column of table 8.

[‡] Number of H₂O blends in region A used for the mini-CG analysis.

[§] χ^2 value for the comparison of the observed and predicted spectra in figure 12.

Table 11. Mini curve-of-growth analysis on CO and H₂O lines in 2MASS 1835+32.

no.	model	$V_{\text{rot}} \sin i^*$	$\log A_{\text{C}}^{(0)\dagger}$	$\log A_{\text{O}}^{(0)\ddagger}$	$\Delta \log A_{\text{C}}^{\S}$	$\Delta \log A_{\text{O}}^{\parallel}$	$\log A_{\text{C}}^{\#}$	$\log A_{\text{O}}^{**}$
1	Bc2280c526	40.8	-3.61	-3.31	-0.101		-3.711 ± 0.128	
2	Bc2280c526	40.8	-3.711	$-3.711+0.3$		+0.008		-3.403 ± 0.024
3	Bc2280c526	40.8	-3.711	-3.403	-0.025		-3.736 ± 0.130	
4	Bc2280c526	40.8	-3.736	-3.403		-0.012		-3.415 ± 0.023
5	Cc2280c526	40.8	-3.61	-3.31	-0.358		-3.968 ± 0.078	
6	Cc2280c526	40.8	-3.968	$-3.968+0.3$		+0.144		-3.524 ± 0.034
7	Bc2280c526	37.6	-3.61	-3.31	-0.184		-3.794 ± 0.094	
8	Bc2280c526	37.6	-3.794	$-3.794+0.3$		+0.033		-3.461 ± 0.036
9	Bc2280c526	44.0	-3.61	-3.31	+0.044		-3.566 ± 0.199	
10	Bc2280c526	44.0	-3.566	$-3.566+0.3$		-0.052		-3.318 ± 0.029
11	Bc2180c528	40.8	-3.61	-3.31	+0.0003		-3.610 ± 0.136	
12	Bc2180c528	40.8	-3.610	$-3.610+0.3$		-0.014		-3.324 ± 0.023
13	Bc2380c525	40.8	-3.61	-3.31	-0.094		-3.704 ± 0.142	
14	Bc2380c525	40.8	-3.704	$-3.704+0.3$		+0.016		-3.388 ± 0.023

* In km s^{-1} . \dagger A starting value for $\log A_{\text{C}}$ in the mini CG analysis. \ddagger A starting value for $\log A_{\text{O}}$ in the mini CG analysis. \S Abundance correction to $\log A_{\text{C}}$ in column 4. \parallel Abundance correction to $\log A_{\text{O}}$ in column 5. $\#$ Resulting abundance $\log A_{\text{C}} = \log A_{\text{C}}^{(0)} + \Delta \log A_{\text{C}}$. $**$ Resulting abundance $\log A_{\text{O}} = \log A_{\text{O}}^{(0)} + \Delta \log A_{\text{O}}$.**Table 12.** χ^2 test on the fittings of the observed and predicted spectra of CO and H₂O in 2MASS 1835+32.

no.	model	$V_{\text{rot}} \sin i^*$	$\log A_{\text{C}}^{\dagger}$	$\log A_{\text{O}}^{\ddagger}$	$\chi^2(\text{CO})^{\S}$	$N_{\text{CO}}^{\parallel}$	$\chi^2(\text{H}_2\text{O})^{\#}$	$N_{\text{H}_2\text{O}}^{**}$
1	Bc2280c526	40.8	-3.711	-3.403	5.803	4	2.035	8
2	Cc2280c526	40.8	-3.968	-3.524	10.369	4	2.879	8
3	Bc2280c526	37.6	-3.794	-3.461	9.406	4	2.568	8
4	Bc2280c526	44.0	-3.566	-3.318	3.126	4	1.820	8
5	Bc2180c528	40.8	-3.610	-3.324	5.682	4	2.074	8
6	Bc2380c525	40.8	-3.704	-3.388	6.016	4	2.099	8

* In km s^{-1} . \dagger $\log A_{\text{C}}$ used for predicted spectrum. \ddagger $\log A_{\text{O}}$ used for predicted spectrum. \S χ^2 value for the fitting of the observed and predicted spectra of CO. \parallel Number of CO blends used in the mini CG analysis. $\#$ χ^2 value for the fitting of the observed and predicted spectra of H₂O in region B. $**$ Number of H₂O blends used in the mini CG analysis.

Table 13. Carbon and oxygen abundances in late M dwarfs.

obj.	$\log A_C^*$	$\log A_O^\dagger$	$\log A_O/A_C$
GJ 54.1	-3.38 ± 0.09	-3.13 ± 0.06	0.25
GJ 752B	-3.55 ± 0.07	-3.31 ± 0.04	0.24
GJ 873	-3.44 ± 0.09	-3.13 ± 0.06	0.31
GJ 1002	-3.42 ± 0.09	-3.17 ± 0.05	0.25
GJ 1245B	-3.44 ± 0.10	-3.15 ± 0.07	0.29
GAT 1370	-3.78 ± 0.06	-3.41 ± 0.06	0.37
LP 412-31	-3.36 ± 0.07	-3.20 ± 0.03	0.16
2MASS 1835+32	-3.57 ± 0.20	-3.32 ± 0.03	0.25
the Sun 1 [‡]	-3.44 ± 0.04	-3.07 ± 0.035	0.37
the Sun 2 [§]	-3.57 ± 0.05	-3.31 ± 0.05	0.26

* From table 6 for the first seven objects and from table 11 (line no. 9) for 2MASS 1835+32.

† The weighted mean of $\log A_O^B$ and $\log A_O^A$ from table 8 and table 10, respectively, for the first seven objects and from table 11 (line no. 10) for 2MASS 1835+32 for which region A is not analyzed.

‡ Anders & Grevesse (1989).

§ Asplund et al. (2009).

Table 14. Spectroscopic data of CO lines (2-0 band).*

Ref. no. [†]	wavelength [‡] (Å)	$\log gf$	L.E.P. (cm ⁻¹)	Rot. ID.
15	23029.797	-5.499	1667.971	R 29
	23029.902	-4.984	9936.531	R 72

* To be added to table 7 of Paper I.

† Ref. no. refers to figure 13b.

‡ In vacuum.